LASER SPIKE ANNEALING OF III-V MATERIALS AND FULL-FIELD THERMAL IMAGING DURING LASER SPIKE ANNEALING

A Dissertation

Presented to the Faculty of the Graduate School

of Cornell University

in Partial Fulfillment of the Requirements for the Degree of

Master of Science

by

Hsien–Lien Huang

Aug 2018

ABSTRACT

Laser Spike Annealing (LSA) is a powerful technique for investigating reaction kinetics at high temperatures in the sub–millisecond time regime. In this regime, significant advantages have been shown in applications of ultra-shallow junction formation in ion–implanted III–V and III–N semiconductor materials. Dopant activation of Si–doped InGaAs and GaN heterostructure was studied using CO_2 and laser diode annealing in sub–millisecond and millisecond timescale. Under LSA, the activation of high–dose implanted dopants was increased in both InGaAs and GaN to peak concentrations comparable (>80%) to the as–implanted dose. During laser annealing, thermodynamic limits were also approached including materials decomposition and damage, which ultimately limited full characterization of the activation behaviors. To better understand the annealing windows, we developed an in–situ characterization technique which matches well with laser annealing for combinatorial and high–throughput characterization; this capability significantly enhances the characterization kinetic dopant activation limitations of III–V and III–N materials.

A complementary approach for temperature profiling of LSA was also developed using a thermoreflectance imaging technique. The temperature dependence of reflectance at short wavelengths was used to determine the in–situ dynamic temperatures during CO_2 LSA. Temperatures were calibrated using optical functions of bulk Si with effects of black–body radiation emission captured at longer wavelengths. Thermoreflectance imaging results were compared with previous results, and show good agreements with direct Pt thermistor measurements and simulations results in both space and time. In the future, thermore-

flectance imaging can be exploited to understand not only impurity interaction in III–V and III–N materials, but also to explore kinetics and phase transformations in meta–stable materials.

BIOGRAPHICAL SKETCH

Hsien–Lien Huang was born on November 8th, 1988 in Taichung City, Taiwan. He spent his high school years at Viator Catholic High School in Taichung City. In June 2012, Hsien–Lien obtained his Bachelors of Science degree at National Chung Hsing University in Chemical Engineering, and joined Omnivision Technologies Inc. as a process engineer to work at Hsinchu, Taiwan, and Shanghai, China. Inspired by industrial experience, he decided to pursue a Master of Engineering degree at Cornell University in Chemical Engineering. In August 2015, he joined Professor Paulette Clancy research group to research on Si dopant diffusion in InAs bulk system using DFT and NEB simulations. In August 2016, he had an opportunity to collaborate with Professor Michael Thompson research group and to continue his second master degree. Hsien–Lien acquired experience in collaboration with Jena and Xing group and IBM Corporation to research on GaN and InGaAs materials. In June 2018, he will obtain his Master of Science degree at Cornell University. Hsien–Lien was motivated and decided to pursue his Ph.D. degree at The Ohio State University in Material Science and Engineering upon graduation. He will research on scanning–transmission electron microscopy (STEM) to study the carrier-defect interactions in nanoscale semiconductors.

This thesis is dedicated to my beloved family and friends

ACKNOWLEDGEMENTS

I hope to express my sincere gratitude to my advisor Professor Michael Thompson for his advice and support of my research. His work and dedication towards research and teaching are inspirational to me, and I want to thank him for always being patient and motivates me when I face challenges.

I am also grateful to my advisor Professor Paulette Clancy for all the guidance and suggestions in my research and future directions. I was encouraged and developed confidence in every presentation in group & subgroup meetings.

I wish to give special thanks to David Lynch, Robert Bell, Alan Jacobs, Johnny Zhang, Aine Connolly, Emily Cheng, Katherine Quinn and Alex Wu in Thompson's group and Mardochee Reveil, Victoria Sorg, Jingyang Wang, Haili Jia and Huang–Ta Chen in Clancy's group. It is my pleasure to work with these friendly and smart people. Their supports have been greatly appreciated.

I also want to thanks my colleagues in Clancy's group, Henry Herbol, Andrew Ruttinger, Ryan Heden, Nikita Sengar and Aaron Chen for fruitful and enjoyable discussions. I learned so much from them in all aspects. I am very thankful for all my friends I have made at Cornell as well.

I give special thanks to all the collaborators: Zongyang Hu and Kazuki Nomoto in Jena–Xing's group at Cornell, Kam–Leung Lee at IBM, Alexander Ruyack in Lal's group, and Dr. Tan Kwan Wee. Thanks to Cornell Center for Materials Research especially Kit Umbach as well as staffs and members from Cornell Nanoscale Facility for the training and resources access.

Finally, I sincerely thank my parents, girlfriend, and my brother for their unfailing love and innumerable sacrifices to support my educational endeavors. It would not have been possible without their confidence and encouragements.

TABLE OF CONTENTS

LIST OF TABLES

LIST OF FIGURES

CHAPTER 1

INTRODUCTION

1.1 Challenges of Dopant Activation in III–V Materials

Since the 1980s, researchers have been attempting to decrease the dimensions of transistors to enhance computing speed and reduce power consumption. In order to maintain Moore's Law, both the properties of the material must be improved and innovative device fabrication techniques must be developed. Both play a key role in the creation of the high performance metal–oxide–semiconductor–field-effect–transistors (MOSFETs).

In comparison to elemental semiconductors based solely on Si, compound–based semiconductors fabricated via crystalline blends of two or more elements from the periodic table, for instance SiGe, GaAs, AlN or InGaAs, exhibit enhanced electronics performance and efficiency. By tailoring the composition, these materials can be engineered to customize properties for next generation electronic devices. This is particularly useful for compound semiconductors where their thermodynamic property allow the formation of multiple ternary and quaternary materials, which offers the potential of designing an ideal material.

1.1.1 Indium Gallium Arsenide

Within compound semiconductor materials, compounds with direct band gaps exhibit significant advantages for applications of transistors, photo-

voltaics, and energy conversion. III–V compound semiconductors, composed of elements from the group III and V of the periodic table, are well–known for their fast electron transport properties and low supply voltage requirements. Among these materials, InGaAs is considered to be one of the most promising candidates for n–type channels and source/drain contacts in very–large–scale integration (VLSI) transistors. This III–V compound materials could replace Si technology since is it has demonstrated ten times faster electron mobility.

Indium gallium arsenide (InGaAs), a ternary zincblende semiconductor, is effectively an alloy of InAs and GaAs. With the combination of high electron mobility of InAs, and the large band gap of GaAs to lower the current leakage, InGaAs can be implemented as an n–type channel material to achieve high speed performance and low power consumption. Standard micro and nanofabrication techniques allow the integration of InGaAs into the processing of current Si technology; conventional lithography and dry etch methods advance its practicabilities. As a result, InGaAs is promising to allow the scaling of electronic devices according to the Moore's Law.

The mobility of charge carriers versus lattice constant for III–V materials and group IV materials (Si and Ge), is shown in Figure 1.1. The electron (red squares) and hole (blue circles) mobilities represent the speed of charge carriers that can move in response to an electrical field. The direction of the arrows represents the charge with compressive biaxial strain, which can also be used to modify the mobility.

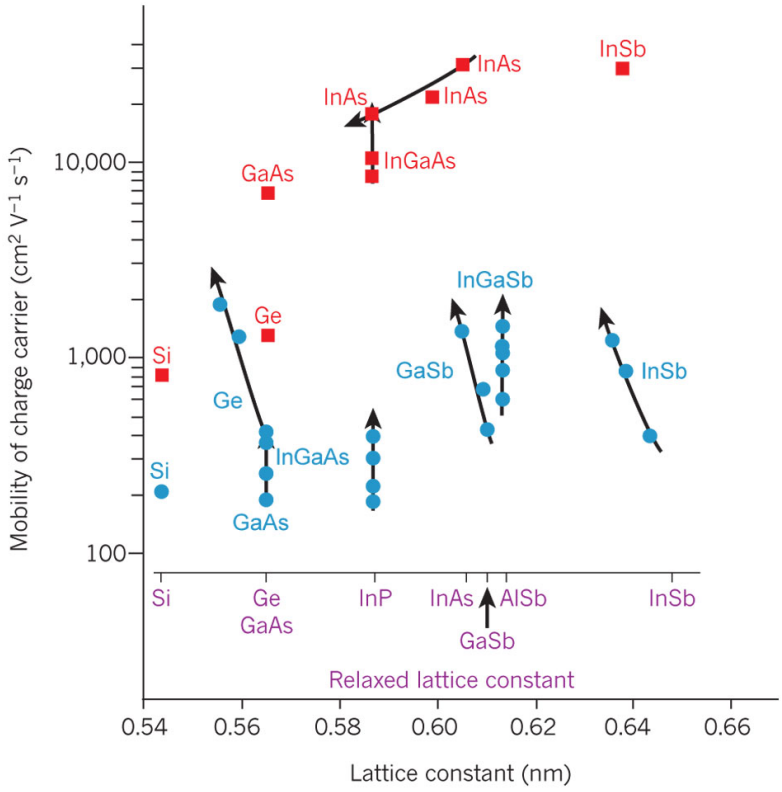

Figure 1.1: The electron mobility (red squares)and hole mobility (blue circles) versus lattice constant for some III–V materials of interest compared to elemental semiconductors like Si and Ge. III–V materials have higher electron mobilities than Si and Ge. Reproduced with permission from del Alamo [3], copyright Nature 2011.

1.1.2 Gallium Nitride

III–N materials, another widely studied group of III–V materials, are defined by a group III elements and the nitrogen as the group V element. By tailoring the composition of a $Al_xGa_{1-x}N$ alloy, direct bandgaps can be extended across the visible light band for emission application at any wavelength. However, this optoelectronic behavior can be hindered by the defects during heterogeneous growth methods, such as metal–organic chemical vapor deposition (MOCVD) or molecular beam epitaxy (MBE). To overcome these growth–related

defect issues, Shuji Nakamura et al. invented a new bottom–up fabrication method to achieve a practical materials for high efficiency blue LEDs. This tremendous breakthrough has been widely recognized and eventually Nakamura's team was awarded the 2014 Nobel Prize in Physics; moreover, this breakthrough has continuously impacted energy savings through power conversion research.

Apart from light emission, gallium nitride (GaN) and other III–N materials also have the advantages of fast carrier transport and high breakdown voltage for power device applications. Current silicon–based devices have power dissipation issues during operation, an issue that can be overcome by wide band gap properties of nitride–based materials. An advanced GaN–based power device with vertical architecture can further improve the performance, efficiency, and cost.

For any of these III–V materials, high performance MOSFETs require dopant activation, which has remained a key challenge for device integration. Thermal processing must control the duration of heating to limit dopant redistribution through impurity diffusion [12]. Thermal processing, in conjunction with ion implantation for tailoring impurity dopant profiles, plays a key role in overall junction device fabrication. Thermal budget is a term that measures the overall effective duration of thermal energy transferred to the sample during elevated temperature processing [13] and must be minimized to limit dopant diffusion. For industrial applications, two types of thermal annealing have been conventionally used. Rapid thermal annealing (RTA) is a typical thermal processing method for the timescales is in the order of seconds with temperature up to 1200 °C. The other is laser spike annealing (LSA), which is studied in this work;

timescales for this method are on the order of sub-millisecond to milliseconds. During LSA, a sample's state is kinetically–limited at high temperature, providing sufficient energy for dopant activations while minimizing dopant diffusion. LSA is also a short timescale annealing technique which allows the anneal area to be localized in space and in time [14]. Both thermal annealing approaches can be implemented in high performance thin film transistors, repairing crystalline damage induced by ion–implantation and achieving high levels of dopant activation.

Over the past decade, industry has applied laser annealing to advanced complementary metal–oxide–semiconductor (CMOS) devices. In 2008, Wang et al. reported the utilization of laser spike annealing can reduce wafer warpage, optimization of pattern density effects, and improvement high–K/metal gate materials [15]. It has also been used to control dopant diffusion with high levels of dopant activation and defect annealing during annealing. The formation of p–n junction for device process integration of Si, SiGe and SOI (Si–on–insulator) substrate has been established [16]. Our studies of dopant activation of III–V materials during laser spike annealing is built on this foundation.

A recent advance in thermal processing is the lateral–gradient laser spike annealing (lgLSA), which has drawn a tremendous amount of attention for rapid characterization of the transient heating on a sub–millisecond time scale [4]. This technique, discussed further in Chapter 2, exploits a lateral non–uniformity in processing condition to rapidly identify optimal condition and processing limits. The technique is used in this work to explore III–V compound materials and high–throughput meta–stable phases explorations [17].

1.2 Laser Annealing for III–V Materials

Laser annealing of III–V materials with pulsed lasers on sub–microsecond time scale have been conducted by several groups.This melt–based laser annealing is in a very different regime from LSA, but provides a context for the challenges in III–V annealing. In 1978, Golovchenko et al. annealed uncapped Te-implanted GaAs with a 12 ns pulsed Q–switched ruby laser (λ = 694.3 nm) [18], and found that the Te has incorporated into the GaAs lattice sites beyond the solubility limitation. In 1979, Sealy, Kular, Badawi et al. laser annealed capped and uncapped Se–doped and Te-implanted GaAs using a 15 – 25 ns pulsed Q-switched ruby laser [19, 20, 21]. The crystalline damage from ion–implantation at high temperature was repaired and achieved carrier concentrations in the range of $1 - 2 \times 10^{19}$ cm^{-3}. In 1986, Barnes et al. laser annealed uncapped Te-implanted GaAs with overlapping 125 ns pulses and claimed to develop the ohmic contacts on the samples [22]. Furthermore, James et al. annealed Zn–doped and Si–doped GaAs using a pulsed CO_2 laser ($\lambda \sim 10\ \mu$m), and increased free carrier absorption as the temperature increased [23]. More recently, Kong et al. laser annealed InGaAs films with a single 23 ns pulsed excimer laser (λ = 248 nm), and annealed damage from implantation while incorporating silicon concentrations nearing 10^{21} Si/cm^3 [24]. They also noted a limitation of RTA at 800 °C to activate dopants before unwanted substrate degradation was observed.

In the case of GaN, Zaldvar et al. monitored the effect of laser annealing with 12 ns ArF excimer laser (λ = 193 nm) [25] on Mg and Si–doped GaN using cathodoluminescence microscopy, and the most intense emission which is compatible with a Mg activation process induced by the laser treatment was observed. In 2000, Lai et al. CO_2–laser annealed Mg–doped GaN films to acti-

vate Mg–doped p–type GaN films [26], and achieved hole concentration of Mg-doped GaN film to approximately 1×10^{17} cm^3 using 7.5 W of the laser power. It has also been shown that Ni films can improve the contact characteristics of laser–annealed p–GaN for overall hole density by the factor of 2 [27]. In 2005, Wang et al. used 248 nm KrF excimer laser irradiation to activate Be–implanted GaN [28], and found the sample retained good crystal quality and dopant activation using pulsed laser annealing followed by RTA. In summary, melt–based laser annealing can be utilized to activate implanted dopants in n and p–type samples, and repair the crystalline damage occurred from implantation. It also allows achieving high carrier concentrations.

1.3 Laser Spike Annealing

1.3.1 System Setup

Two laser spike annealing systems, a 130 W far–infrared CO_2 laser (= 10.6 μm) and a 250 W fiber–coupled near–infrared diode laser (λ = 980 nm), were installed for millisecond and sub–millisecond annealing at Cornell. A linear motion stage is capable for traveling up to 400 mm/s. The laser system setup is shown in Figure 1.2, where the red line represents the beam path for the CO_2 laser while the green line represents the optical fiber coupling the 980 nm beam. For all the following experiments in this thesis, laser scans were performed on this setup.

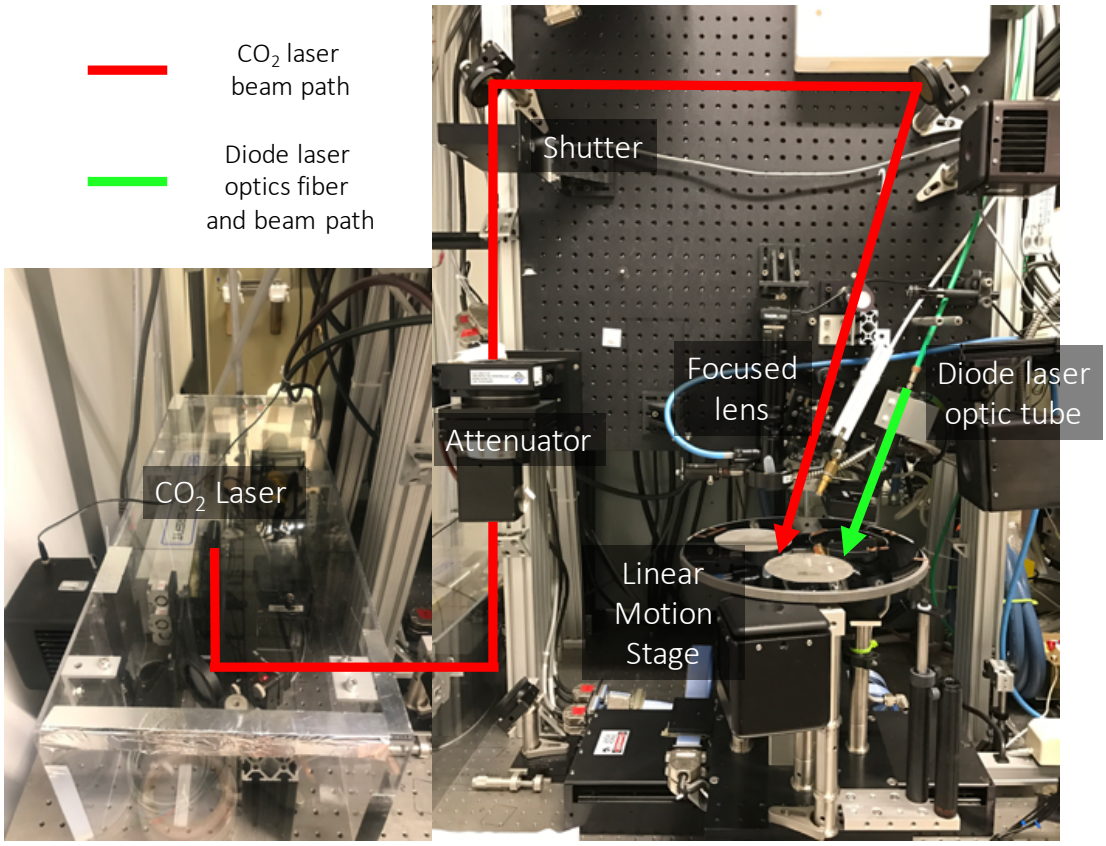

Figure 1.2: Laser spike annealing system at Cornell

1.3.2 Concepts

Traditional annealing approaches, such as furnace and rapid thermal annealing (RTA), use thermal energy to activate the dopants in InGaAs [29] and GaN [30] on timescales from seconds or even up to hours. In contrast, laser spike annealing (LSA) reaches much higher temperatures within shorter time span, as shown schematically in Figure 1.3. With rapid heating and quenching rates of 10^4 – 10^7 K/s using LSA, sufficient thermal energy can be provided to allow intrinsic defects to be removed, and to dissolve any existing dopant defect clusters. Since LSA also operates on a short timescale compared with traditional annealing methods, there is limited dopant diffusion.

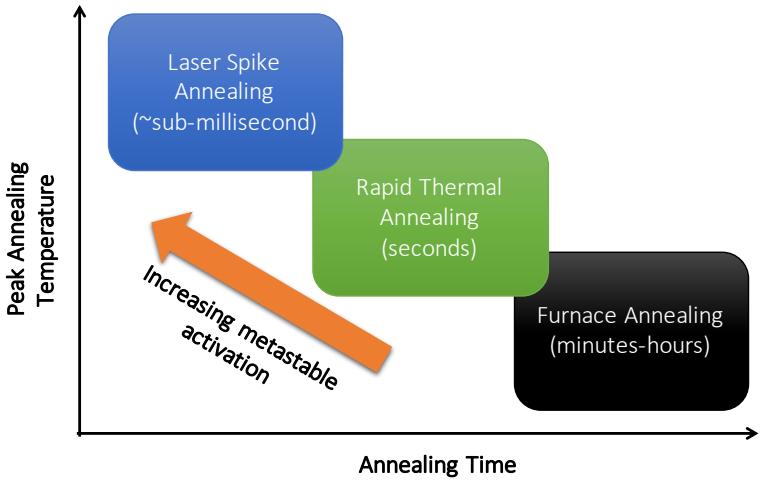

Figure 1.3: Different thermal annealing approaches in terms of temperature and time scales.

Laser spike annealing potentially enables dopants sitting in metastable states to reach favored substitutional sites while preventing long–range diffusion. There are three controlled parameters : (i) the wavelength of the laser irradiation, (ii) the speed for a single laser scan over the stage, and (iii) the laser intensities. The lateral gradient laser spike annealing (lgLSA) technique is a powerful combinatorial technique to characterize conditions rapidly and identify a target annealing temperature (Figure 1.4, left). By profiling the scan direction, the effect of annealing temperature from unannealed (far away from the center of the laser scan) to the highest annealing temperature (middle of the scan) as a function of position on the sample (Figure 1.4, right) can be obtained [4].

The annealing time is characterized as dwell (τ_{dwell}) time, which is defined as the full–width–half–max (FWHM) of the laser focus in the scan direction divided by the velocity of the moving stage (e.g., 88.4 m FWHM/ 88.4 mm/s = 1 ms dwell). Typically, dwell time ranges from 150 μs to 10 ms. The laser can couple with a substrate, thin film, stack or absorber layers. However, the critical

parameters for the laser coupling are the absorption and reflectivity of the material at the laser wavelength. These optical and thermal properties are strongly temperature dependent and impacting thermal calibrations [31].

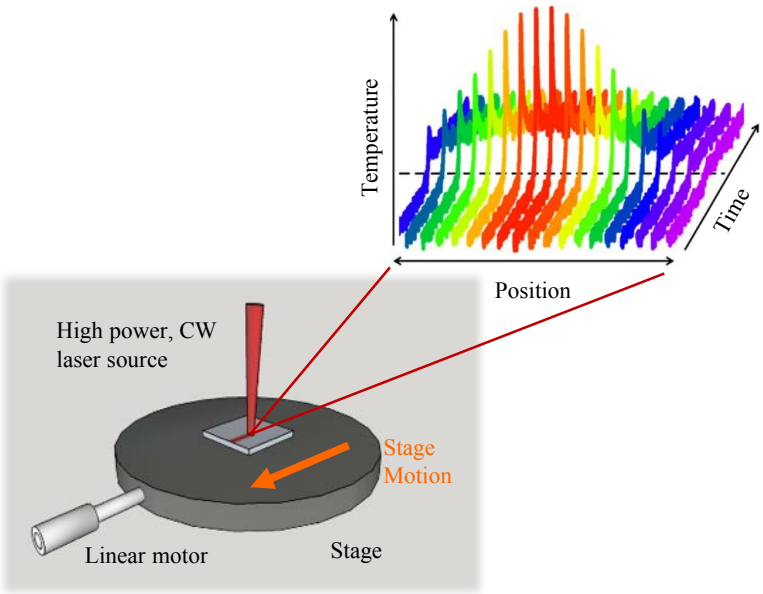

Figure 1.4: Schematic of the single scan laser annealing set-up (bottom left) and temperature profile as a function of position across the scan width (top–right). The laser scanned over the sample creates a temperature gradient based on the sample position. Reprinted with permission from Bell et al. [4]. Copyright 2016 American Chemical Society.

1.3.3 Laser Sources

Almost any continuous wave lasers can be used for LSA. For this work, two infrared lasers were used. One was a CO_2 laser (P_{max}= 130 W, λ = 10.6 μm) and the other was a diode laser (P_{max} = 250 W, λ = 980 nm). In the case of the CO_2 laser, the beam was focused on maintaining a broad Gaussian shape in the x–direction and a narrow Gaussian shape in the y–direction, as shown in Figure 1.5 (a). The x–axis of the diode beam was focused on achieving a profile with a

roughly flat top with the y–axis focused to a Gaussian shape, see Figure 1.5 (b). The lasers are scanned in the direction of the short axis, in this case, the y–axis.

The choice of a laser source for LSA is determined by the interactions in the materials. If the photon energy of laser is large enough, photons excite electrons across the bandgap. For lower energy photons, absorption is based on lattice oscillation and vibrations induced by excited electron–electron, electron–phonon, and electron–plasma interaction.

The summary of optical properties for semiconductor material is presented in Table 1.1. The conversion between wavelength and energy is shown in Equation 1.1:

$$E = \frac{hc}{\lambda} \tag{1.1}$$

where E is the energy, h is Planck's constant, c is the speed of light, and λ is the wavelength (hc = 1240 in units of eV–nm). If the direct band gap of material is less than the energy of the laser, the sample can directly absorb laser energy by band–to–band excitations. The absorption coefficient can be determined by Equation 1.2:

$$\alpha = \frac{4\pi k}{\lambda} \tag{1.2}$$

where k is the extinction coefficient and λ is the wavelength. Therefore, the absorption length can be defined as 1 / α, as shown in Table 1.2. It is evident that the energy of the light from the CO_2 laser will not heat any of the samples by direct band gap absorption, but the 980 nm diode laser can directly couple

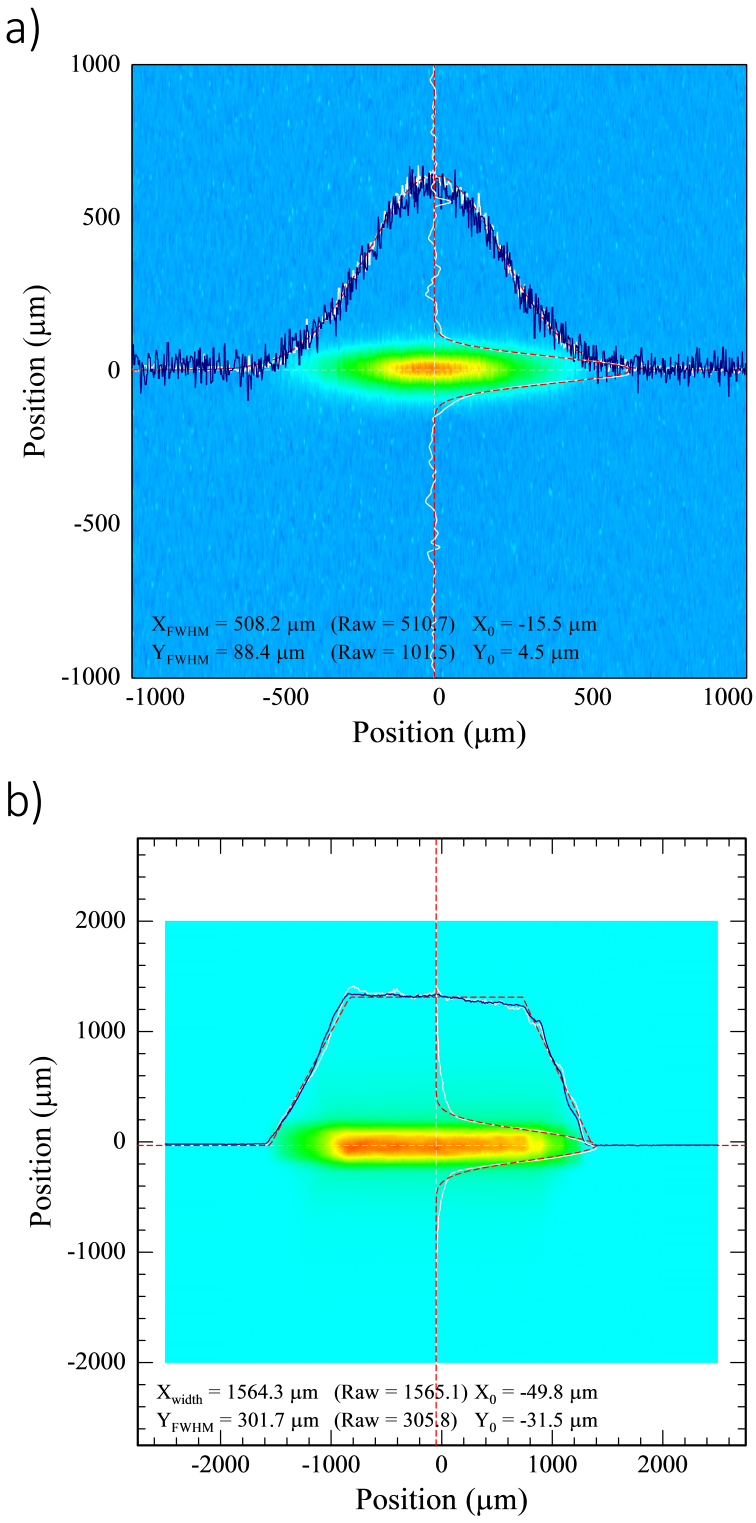

Figure 1.5: Laser intensity profile for the (a) CO_2 laser and the (b) diode laser. In both cases, the laser is scanned in the y–direction to quickly heat and quench the samples. The x–axis is focused to allow for spatially resolved temperature measurements

with either $In_{0.53}Ga_{0.47}As$ or InAs. It is also significant that the capping layers added to the sample may alter the interaction.

Table 1.1: Summary of the direct band gap of III–V materials used in this study and the energies of the lasers used to anneal them. For direct band gap light absorption, the material must have a band gap energy that is smaller than the energy of the light.

		Energy Bandgap [eV]	**Wavelength [nm]**
Lasers	CO_2	0.12	10600
	Diode	1.27	980
Materials	Si	1.12	1107
	InGaAs	0.75	1653
	GaAs	1.42	871
	InAs	0.35	3503
	InP	1.34	923
	GaN	3.39	365
	AlN	6.2	200
	Ga_2O_3	4.8	258
	Al_2O_3	9.90	125
	Si_3N_4	5.0	248

1.3.4 Temperature Calibrations

Several techniques have been implemented for this temperature calibrations in our group: the thermal decomposition behavior of the block copolymer [32], phase changes [4], and patterned resistors [31]. Methods used in this thesis will be discussed in Chapter 2.

Table 1.2: Summary of optical properties for semiconductor materials. The optical properties are dependent on the wavelength of light used. The most practical parameters are absorption length ($1/\alpha$) and reflectivity (R). A small absorption length means that the sample strongly absorbs the light. Additionally, lower reflectivity allows more light to be absorbed by the sample.

Materials	**Laser Energy [eV]**	**Refractive Index (n)**	**Extinction coefficient (k)**	**Reflectance (R)**	**Absorption Coefficient (α) [cm^{-1}]**	**Absorption Length [μm]**
Si	0.12	3.42	1.23×10^{-4}	0.30	1.50	6672.89
	1.3	3.59	1.00×10^{-3}	0.32	131.74	75.90
InGaAs	0.12	NA	NA	NA	NA	NA
	1.3	3.66	0.288	0.33	3.79×10^{4}	0.26
GaAs	0.12	3.272	NA	0.28	NA	NA
	1.30	3.65	0.074	0.32	9749.07	1.03
InAs	0.12	3.40	2.1×10^{-4}	0.30	2.55	3915.72
	1.3	3.71	0.432	0.34	5.69×10^{4}	0.18
InP	0.12	3.04	1.3×10^{-4}	0.26	1.58	6325.39
	1.3	3.36	2.9×10^{-4}	0.29	38.21	261.74
GaN	0.12	1.814	1.8×10^{-2}	0.084	218.9	45.7
	1.3	2.230	4.97×10^{-2}	0.145	6543.6	1.53
AlN	0.12	1.814	1.8×10^{-2}	0.084	218.9	45.7
	1.3	2.230	4.97×10^{-2}	0.145	6543.6	1.53
Ga_2O_3	0.12	NA	NA	NA	NA	NA
	1.16	1.916	NA	0.0986	NA	NA
Al_2O_3	0.12	0.77	0.108	0.02	1308.04	7.65
	1.3	1.75	0.02	0.07	2634.88	3.80
Si_3N_4	0.12	1.78	1.39	0.26	16878.26	0.59
	1.3	2.00	NA	0.11	NA	NA

1.3.5 Challenges

Since all of the existing temperature characterization tools are local spot measurements, it is hard accurately determine the annealing temperature during LSA. This is an even greater challenge during lgLSA since each position is heated to significantly different temperature. Thermal characterization techniques to quantify the temperature with good spatial resolution are necessary for LSA, and some optical characterization tools such as infrared (IR) thermography [33, 34, 35], micro–Raman [36] and thermoreflectance [37, 38] show good results in measuring the surface temperature with high spatial resolution. Thus, multiple thermal characterization techniques are further discussed in the next section.

1.4 Thermal Characterization Techniques

In the late twentieth century, thermal measurement techniques were developed to measure the absolute or relative temperatures of electronic devices or detect the thermal properties of materials [39, 40]. These characterizations [41, 42] include micro–thermocouple, infrared (IR) thermography [43], thermoreflectance [44], scanning thermal microscopy (SThM) and fluorescence thermography. So far, IR thermometry has been the most widely used technique for temperature measurements of electronic devices, particularly in integrated circuits (IC). However, the low resolution($\sim 3\ \mu$m) and a low emissivity of metals limit the application of IR thermography. Micro–thermocouples contain inexpensive point measurement contact probes which can provide accurate temperature readings with a thermal resolution of 0.01 K. However, large thermocou-

ple wires could cause low resolution as well. By fabricating a thermocouple on the tip of an Atomic Force Microscopy (AFM) cantilever, the SThM technique has very high spatial resolution ($\approx 0.05\ \mu$m) with a thermal resolution of 0.1 K. However, the roughness of the sample surface can cause variations in the tip–surface thermal contact, leading to noise in the thermal signals.

One of the most promising techniques is thermoreflectance measurements of temperature based on small changes in surface reflectance. These techniques can be implemented using high resolution CCD cameras to provide direct spatial images of temperature profiles. Thermoreflectance spectroscopy has been previously utilized in point–based laser scanning methods and with multi–point detection systems. Temperature resolutions can be as low as 10 mK with spatial resolutions of 250 nm. This technique is also applicable for studying thermal transients and heat transfer in thin films and low dimensional structures such as multilayers and superlattices. Therefore, the integration of CCD–based thermoreflectance spectroscopy with laser spike annealing is a promising method for exploring of temperature profiles in III–V and III–N materials.

Table 1.3 summarizes various methods for high–resolution thermal measurements which are suitable for micro and nanoscale semiconductor devices [1]. Note that some of these techniques rely on the integration of device coating and surface effectiveness to measure absolute or differential temperature in different spatial, thermal, and temporal resolution.

Table 1.3: Summary of high–resolution thermal measurement techniques in micro and nanometer range [1]

Method	**Principle**	**Resolution**			**Imaging**
		Spatial (μm)	Temperature (K)	Response time (μs)	
Microthermocouple	Seebeck effect	50	0.01	10^7 – 10^8	No
Infrared thermography	Planck blackbody emission	3 – 10	0.02 – 1	20	Yes
Liquid crystal thermography	Crystal phase transitions change color	2 – 5	0.1	10^8	Yes
Thermoreflectance	Temperature dependence of reflection	0.3 – 0.5	0.01	0.006 – 0.1	Yes
Scanning thermal microscopy (SThM)	Atomic force microscope with thermocouple or Pt thermistor tip	0.05	0.1	10 – 100	Scan
Fluorescence thermography	Temperature dependence of quantum efficiency	0.3	0.01	200	Scan
Optical interferometry	Thermal expansion, Michelson type	0.5	0.0001	0.006 – 0.1	Scan
Micro–Raman	Shift in Raman frequency or ratio of Stokes/anti–Stokes amplitudes	0.5	1	1	Scan
Near field probe (NSOM)	Use near field to improve optical resolution	0.05	0.1 – 1	0.1 – 10	Scan
Built–in temperature sensors	Fabricate a thermal sensor integrated into the device	>100	0.0002 – 0.01	1	No

1.5 Thermoreflectance

Since all of the existing temperature characterization tools during LSA are local spot measurement, CCD imaging–based thermoreflectance emerged for its high–resolution and non–contact characteristics, which can be useful for mapping of temperature distribution, thermal transient measurement, hot spot detection, optical characterization of photonic devices, failure analysis of electronic devices and measurement of thermal conductivity in thin films. The notion of the TR technique is based on the variation in the reflectivity (ΔR) of a surface as a function of the change in temperature (ΔT) through the following relation:

$$\frac{\Delta R}{R} = \left(\frac{1}{R}\frac{\partial R}{\partial T}\right)\Delta T = \kappa \Delta T \tag{1.3}$$

The thermoreflectance coefficient (κ) is the relative change in optical reflectance per unit temperature change, and standard values for metals and semiconductors are in the orders of 10^{-6}–10^{-4} K^{-1}. Bruno Batz was the first to report the thermoreflectance spectra of germanium [45]. Matatagui then presented the thermoreflectance spectra of semiconductors including Si, GaAs, InAs and other compound alloys in 1968 [46]. Later, in 1993, a detailed characterization of thermal properties of diode lasers using thermoreflectance was reported by Epperlein [47]. Since then, thermoreflectance has been applied to the investigation of diode lasers [48], integrated circuits [49], transistors and solar cells. Thermoreflectance has also be used to determine the thermal conductivity of thin films by using pump–probe TR. This is based on heating the samples with a short laser pulse (pump) and measuring the temperature decay from the intensity variation

of the reflected beam (probe) [50, 51]

Thermoreflectance measurements can be realized in two experimental configurations: the point–based laser scanning method in which a laser beam is probed and captured by a photodiode detector [52], or a LED illuminator is used to produce the probe light (spectrally narrow), and the whole thermal image is stored in one snapshot [53, 40]. The typical experimental setup for a laser–based and a CCD–based thermoreflectance is shown in Figure 1.6. The other is a classical, focused laser beam configuration [50, 54] which uses the laser line appropriate for examining the structure as a probe beam and registers the thermal image by scanning the sample surface point by point. In this thesis, we used CCD thermoreflectance to perform thermal characterization with complementary analysis.

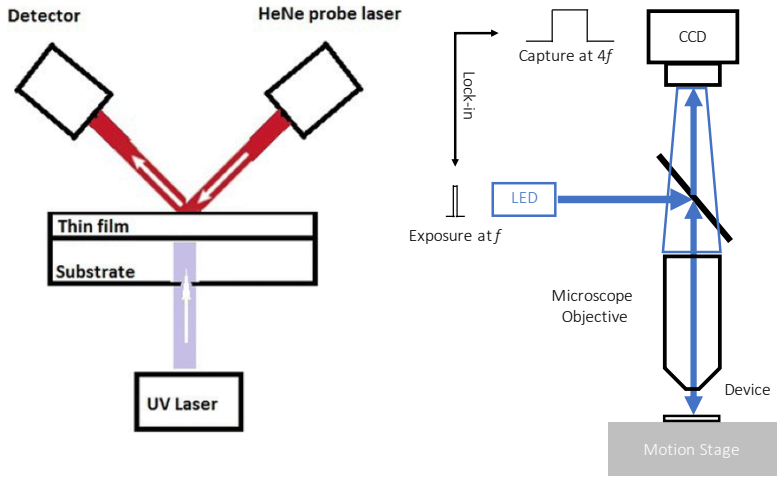

Figure 1.6: Schematic depiction of a laser–based and a CCD–based thermoreflectance spectroscopy setup.

1.6 Thesis Overview

This thesis focuses on two aspects of laser spike annealing: (i) high–temperature, short timescale heating with lasers on III–V materials, for instance InGaAs and GaN, to understand the limitation of annealing states which are inaccessible to longer timescale methods, and (ii) a new full field calibration with high–throughput, transient and non–contact approach to map full temperature field in single image. Additionally, the thermal fields of annealing temperatures were quantified as a function of temperature in semiconductors, especially in silicon. This analysis enabled probing optically on the material surface and was capable compared with other ex–situ thermal characterization methods, including polymer decomposition, Au nano–dots melting and Pt thermistors calibrations.

CHAPTER 2

REVIEW OF KEY CHARACTERIZATION TECHNIQUES

2.1 LSA Temperature Calibration

Absolute temperature have been characterized in our lab using three ex–situ and in–situ methods : (i) polymer decomposition, (ii) Au dots melting, and (iii) Pt thermistor measurements. For low temperature LSA, polymer decomposition was used to identify annealing temperatures from 650 °C to 1050 °C. The dwell–dependent thermal decomposition behavior of a 60 nm block–copolymer poly(styrene–block–methyl methacrylate), 70 wt.% polystyrene [31, 32] thin film was compared to well–calibrated behavior on heavily doped Si substrates. A schematic of polymer decomposition for temperature calibration on heavily doped Si wafer is shown in Figure 2.1. For the CO_2 laser, the peak annealing temperature ranges from 700 °C to 1000 ° C with dwells ranging from 250 μs to 2 ms (250 μs, 500 μs, 1 ms, 2 ms). For the diode laser, the peak annealing temperature ranges from 700 °C to 1000 °C, and the dwells ranged from 250 μs to 5 ms (250 μs, 500 μs, 1 ms, 2 ms, 5ms). The change in thickness as a function of position was converted to a function of laser annealing temperature using the profile from well–characterized Si–based Pt thermistor measurements. The polymer decomposition widths were characterized using a profilometer (KLA-Tencor), as shown in Figure 2.2.

Gold microdot melting was used to determine the annealing condition where the temperature reached 1064 °C, the melting point of Au. Approximate 25 nm of Au dots on a 10 μm lateral space, were thermally deposited onto 50 nm PECVD (Plasma–enhanced chemical vapor deposition) SiO_2–coated sam-

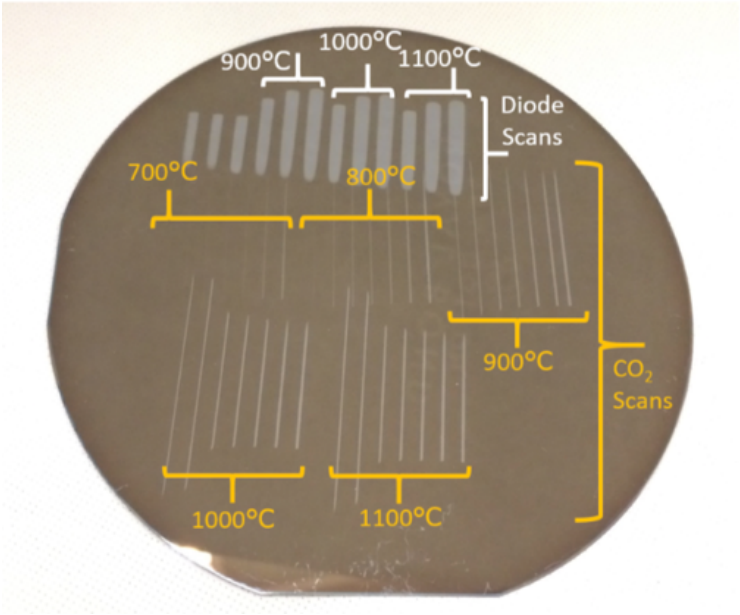

Figure 2.1: Absolute temperature calibration for laser annealing using polymer decomposition on a well–calibrated, heavily doped silicon wafer

ples. As the laser heats the sample above the melting temperature of gold, the dots de-wet into smaller particles due to surface tension. A example for laser annealing of gold dots on InGaAs sample is shown in Figure 2.3, with the sample temperature exceeding the gold melt. Another example for laser annealing of gold dots on GaN surface is shown in Figure 2.4, with the temperature elevated much higher than the material damage (~ 2000 °C). The temperature of InP melt is similar to that of Au melt, which was then determined by using this method.

Platinum thin film resistors, or Pt thermistor, were used to develop relative temperatures as a function of laser power, and across the laser scans for lgLSA. These thermistors were fabricated on 50 nm PECVD SiO_2–coated Si wafers to electrically insulate the sample from thermistors, as shown in Figure 2.5. Resistance was measured using a 4–wire technique, with the current measured

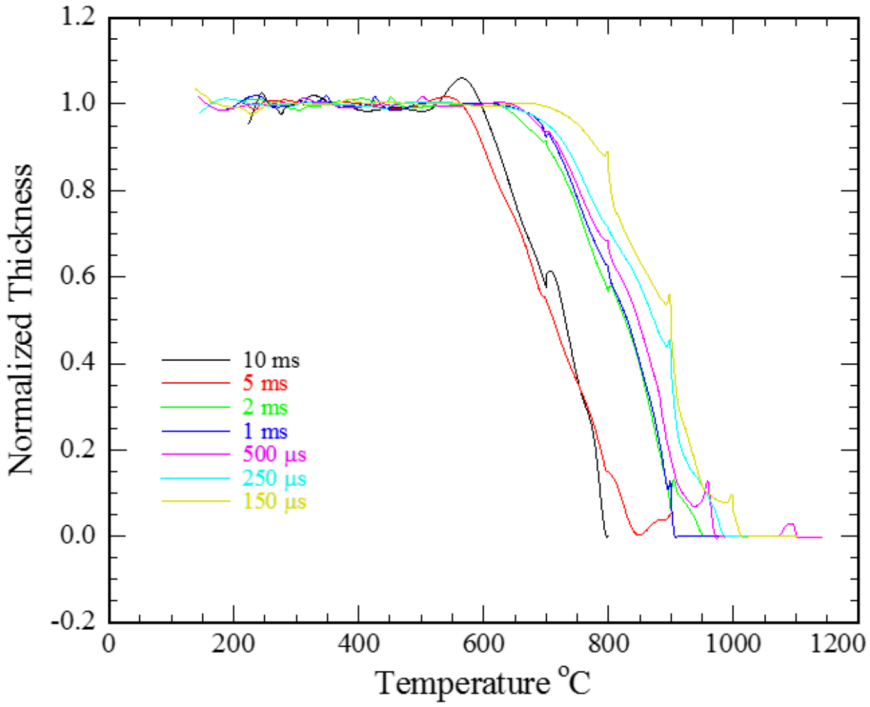

Figure 2.2: The laser annealing absolute temperature calibration using polymer decomposition on a well–calibrated, heavily doped silicon wafer. Data show the change in thickness as a function of peak annealing temperature for various dwells

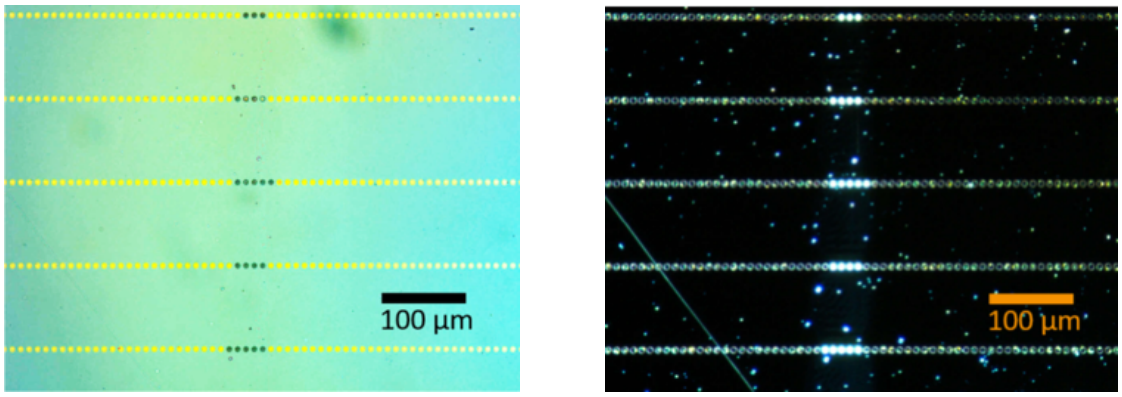

a) Bright Field b) Dark Field

Figure 2.3: Absolute temperature calibration for the laser annealing of InGaAs films using the melting temperature of gold as the reference

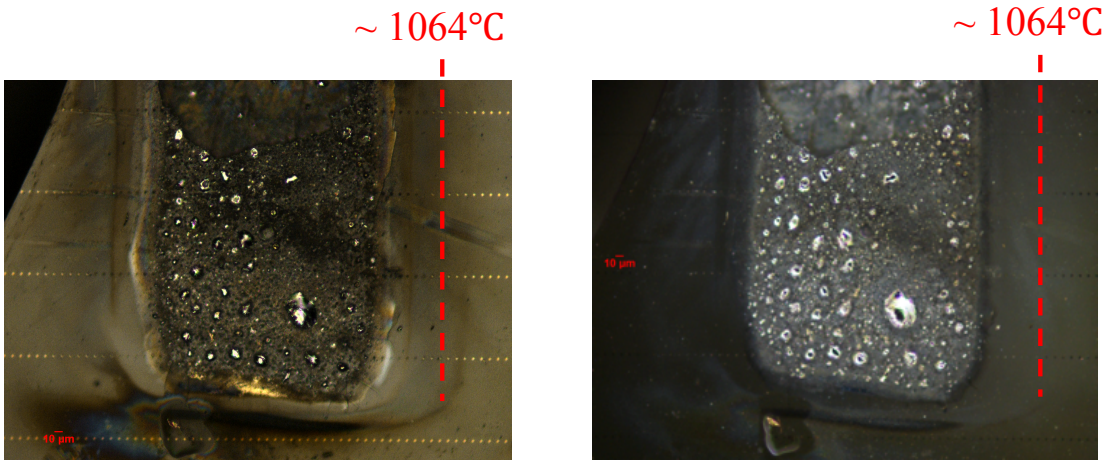

Figure 2.4: Absolute temperature calibration for the laser annealing of GaN films using the melting temperature of gold as the reference

through the outer two leads and the voltage measured through the inner two leads. Therefore, the peak temperatures as a function of laser power against the maximum resistance in each dwell could be observed. Additionally, the lateral temperature across the laser scans was determined by translating the probe average 20 μm across the profile up to the peak temperature ~ 1414 °C on Si.

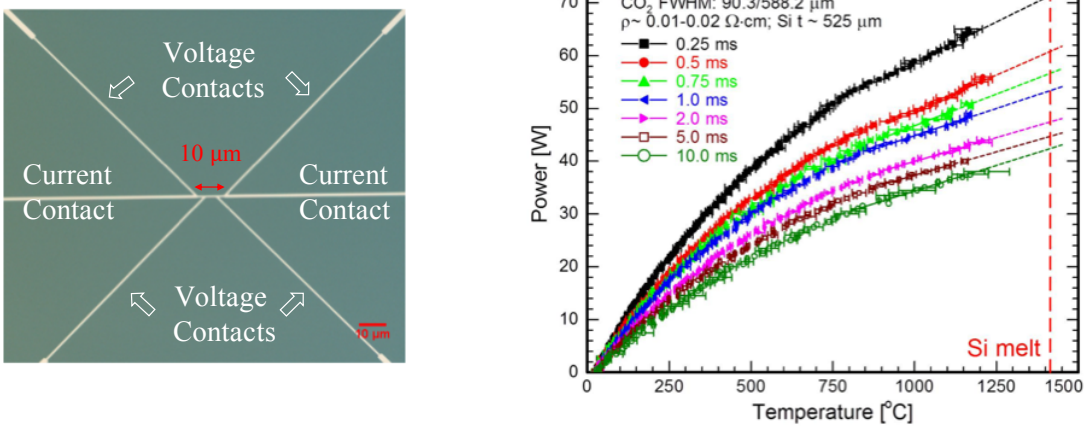

a) Pt thermistor

b) CO_2 peak temperature

Figure 2.5: (a) A bright field micrograph of the Pt thermistor fabricated on Si (b) CO_2 temperature calibration shown for dwell times ranging from 250 s to 10 ms

2.2 Raman Spectroscopy

2.2.1 Principles

Raman spectroscopy is a useful tool to observe vibrational, rotational and phonon excitations properties of materials. The principle is based on inelastic energy changes as shown in Figure 2.6. A single wavelength laser illuminates the sample, and the photons excite electrons from one state to a virtual energy state, which subsequently relax to a different state. Most of the photons are elastically scattered with no change in wavelength, a phenomenon called Rayleigh Scattering. However, a small fraction of the light is scattered inelastically to a different wavelength with a shift in energy called Raman Scattering. In Stokes Raman Scattering, photons lose energy to the crystal phonons (lattice vibrations) and local vibrational modes from defects, whereas photons gaining energy from the phonon system are defined as anti–Stokes Raman Scattering. The changes in wavelength of the scattered photons provides chemical and structural information of the sample. Therefore, Raman spectroscopy is a powerful technique to ”fingerprint” the properties of materials based on the identification of vibrational modes corresponding to the specific molecular motions in the materials.

2.2.2 System Setup

In this work, a 488 nm laser source was installed in a Renishaw InVia micro-Raman system in the backscattering configuration with a one μm probe diameter, as shown in Figure 2.7. This configuration was chosen based on the depth

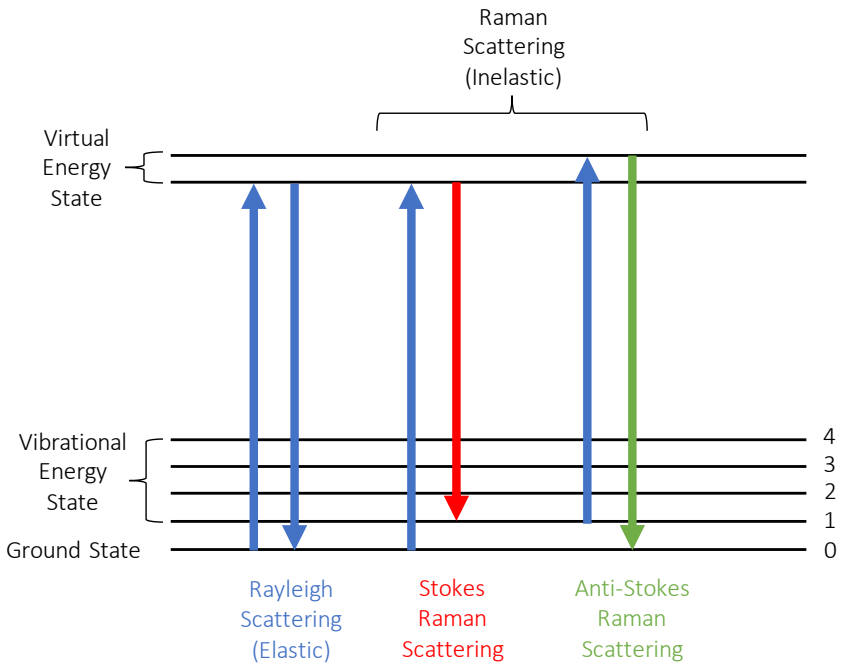

Figure 2.6: Schematic of principle of Raman scattering with regards to the elastic Rayleigh Scattering (blue) and, the inelastic Stokes (red) and anti–Stokes Raman Scattering (green)

penetration of the laser light. The lateral spatial resolution can be defined as 1.22 λ / NA, where λ is the wavelength of the illuminating light and NA is the numerical aperture (which is equal to $nsin(\theta)$, where n is the index of refraction of the medium (1.0 in the case of air) and θ is the half angle subtended by the optics). For our configuration, the blue laser at 488 nm with a 0.90/100x objective, the spatial resolution is 661 nm.

The exposure times of laser beam on the sample, and the number of accumulations, influences the signal–to–noise ratio. Longer exposure time and dense accumulations can achieve adequate sensitivity. In case of InGaAs studies, 45 s exposure time and three accumulations were used; while 10 s exposure times and one accumulations was used for GaN research.

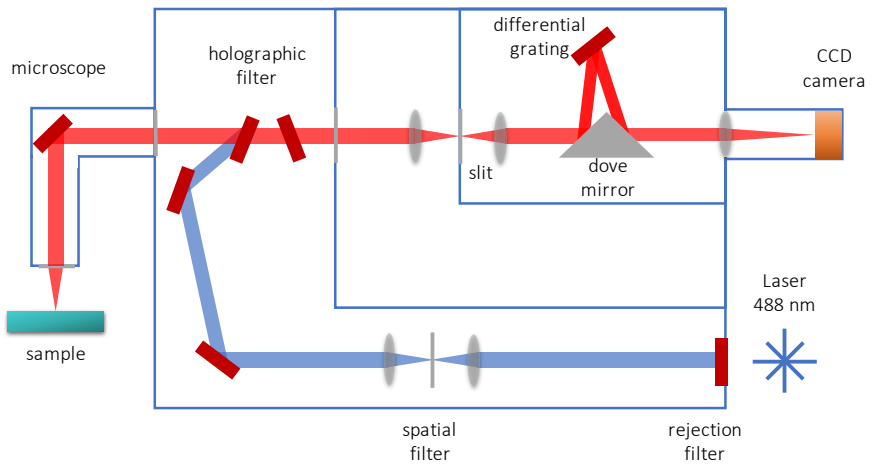

Figure 2.7: Schematic layout of Renishaw Raman confocal microscopy

2.2.3 Raman Scattering by LOPCMs

The free–charge density (N_e) in doped polar semiconductors can be analyzed with the longitudinal–optical (LO)–phonon–plasmon coupled modes (LOPCMs). In general, two branches of the coupled modes labeled L^+ and L^- are observed in high–mobility n–type binary semiconductors. In degenerate materials, a high–frequency mode L^+ has a plasmon–like character and its frequency increases as $N_e^{\frac{1}{2}}$. In contrast, a low–frequency coupled mode (L^-) presents a phonon–like character and approaches the transverse optical (TO) frequency, which is visible for $N_e \simeq 10^{18}$ cm^{-3}. The frequency of LOPCMs correlate with the zeros of wavevector and wavenumber dependent (q, ω) dielectric function of the material, as shown in equation 2.1 [55, 56]:

$$\epsilon(\omega) = \epsilon_\infty + 4\pi(\chi_I + \chi_e) = 0 \tag{2.1}$$

where χ_I is the dielectric susceptibility of the ionic lattice shown in equation 2.2, and χ_e is the dielectric susceptibility of the free–carrier plasma shown in

equation 2.3. By combining equation 2.2 and 2.3, the frequencies of LOPCMs can be determined through equation 2.4.

$$\chi_I = \left(\frac{\epsilon_\infty}{4\pi}\right)\left(\frac{\omega_{LO}^2 - \omega_{TO}^2}{\omega_{TO}^2 - \omega^2}\right) \tag{2.2}$$

$$\chi_e = \left(\frac{\epsilon_\infty}{4\pi}\right)\left(\frac{\omega_p^2}{\omega^2}\right) \tag{2.3}$$

$$\omega_\pm^2 = \frac{1}{2}\left[\omega_{LO}^2 + \omega_p^2 \pm \sqrt{\left(\omega_{LO}^2 + \omega_p^2\right)^2 - 4\omega_p^2\omega_{TO}^2}\right] \tag{2.4}$$

2.2.4 Raman Scattering of InGaAs

LOPCMs have been investigated in many III–V semiconductors, and the carrier density derived from Raman spectrum analysis has been shown to be in good agreement with Hall–effect measurements. A typical InGaAs spectrum is shown in Figure 2.8. For InGaAs, the primary phonon modes include InAs longitudinal optical (LO), GaAs LO, disorder peaks R*, GaAs transverse optical (TO) and InAs TO peaks, as shown in Table 2.1 [2]. The area of the GaAs–like LO peak was used to quantify the crystallinity of intrinsic samples, and the carrier activation of implanted samples. During thermal annealing, inelastically scattered phonons couple with plasmons, reducing the GaAs LO phonon mode and increasing the intensity of the LOPCMs peak. The LOPCM peak, which is typically located between 600 – 1500 cm^{-1}, was used to quantify the active carrier concentration above 10^{17} cm^{-3}, as shown in Figure 2.9.

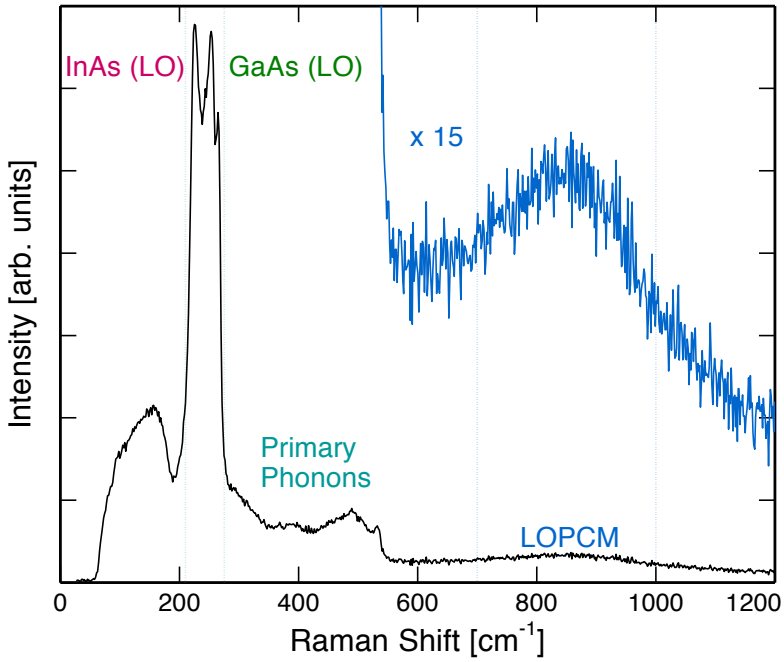

Figure 2.8: Typical InGaAs Raman Spectrum presented with location of the InAs LO (red), GaAs LO (green) and LOPCMs (blue) peaks.

Table 2.1: Primary phonon modes of InGaAs [2]

Primary Peaks	**Peak Positions [cm^{-1}]**	**Allow Modes in (100)**
InAs LO mode	242	Yes
GaAs LO mode	295	Yes
R*	244	Yes
InAs TO mode	218	Forbidden
GaAs TO mode	270	Forbidden

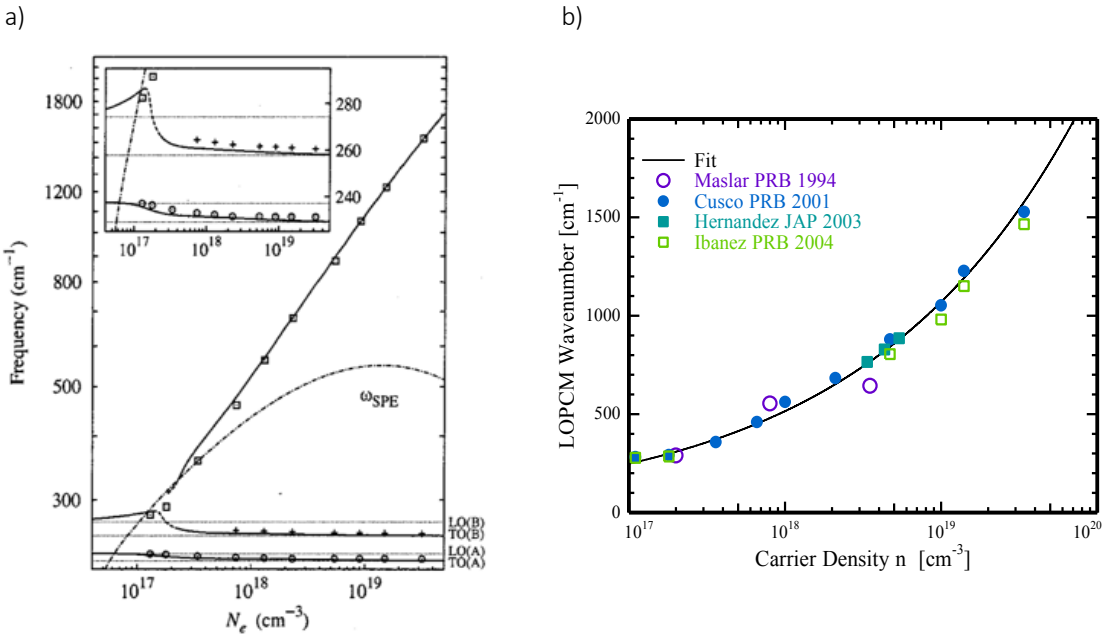

Figure 2.9: Raman wavenumber corresponding to n–type carrier concentrations for InGaAs. In (a), the solid line is the computational solutions, and the points are experimental measurement for carrier–coupled modes derived by Cusco et al [5]. Three coupled modes rise from low (◦) to intermediate (+) and high frequency (□). The dotted line represents the primary LO and TO phonon modes of A for InAs–like and B for the GaAs–like modes. Reproduced with permission from Cusco et al. [14], copyright Physical Review B 2001. In (b), the curve identifies the power law fit to data used to convert the high frequency peak position to carrier concentration, based on modeling of data from [5]. The points are taken from the literature (◦ [6], • [5], ■ [7], and □ [8]).

2.2.5 Raman Scattering of GaN

GaN has six primary phonon modes including A_1, $B_1(B_1^L, B_1^H)$, E_1, and $E_2(E_2^L, E_2^H)$ modes, as shown in Table 2.2 (left) [3]; B_1 modes are Raman inactive (silent modes). Since the incident and scattered light taking z–direction along the c-axis, the A_1 (LO) mode can be observed from backscattering from the c–plane of

wurtzite GaN samples. On the other hand, the E_1 mode can only be observed in the crossed polarization geometry which is perpendicular to c–axis. Therefore, only two E_2 phonon peaks (E_2^L, E_2^H) and one LO phonon peak, A_1 (LO), can be observed as primary modes in the GaN spectrum.

Table 2.2: Primary phonon modes of GaN [3]

Primary Modes	**Peak Positions [cm^{-1}]**	**Local Vibrational Modes**	**Peak Positions [cm^{-1}]**
E_2^L	144	LVM vacancy related defects	360, 420, 670
A_1 (TO)	531	Mg–N	260, 657
E_1 (TO)	560	H–decorated defects	2128, 2147, 2165, 2184, 2198, 2202, 2218
E_2^H	568	Mg–N–H	3123
A_1 (LO)	734		
E_1 (LO)	741		

For the LOPCMs of GaN, it consists of upper and lower–frequency branches, which are denoted as L^+ and L^-, respectively. Figure 2.10 shows the spectrum corresponding to n–type carrier concentration. Since the low frequency–coupled modes (L^-) is extensively sensitive to low carrier density and high frequency–coupled mode (L^+) is more sensitive to the high carrier concentration regime, the LOPCMs can be used to characterize the free–electron density in bulk substrate and impurities–implanted GaN samples.

If a substitutional impurity defect replaces a host–lattice atom that is heavier than the impurity, atomic oscillation may be induced in a limited range around the defect, which is so–called the local vibrational modes (LVMs). On the other hand, the vibrational modes of impurities which are lighter are more localized and can be detected at a higher frequency. Typical LVMs are shown in Table

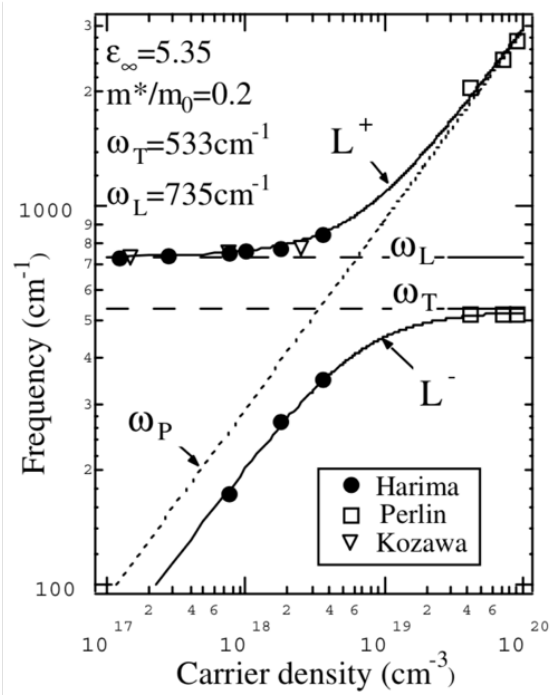

Figure 2.10: The LOPCMs wavenumber corresponding to carrier concentration for n–type GaN [18], summarized from various previous studies of Harima et al (•) [9], Perlin et al (□) [10], and Kozawa et al (▽) [11]. The plasma frequency (ω_p) are marked with dotted line, and the dashed lines represent as the LO mode (ω_L) and TO mode (ω_T). The low frequency–coupled mode (L^-) and high frequency–coupled mode (L^+) are shown as solid curves. Reproduced with permissions from Harima, copyright Journal of Physics: Condensed Matter 2002.

2.2 (right). The critical LVMs in this work is the Mg–N bonding, which can be observed at 657 cm^{-1} as Mg dopant activation for hole conductivity in p–type GaN samples grown by MOCVD and MBE procedures. In addition, the defect–induced modes of LVMs assigned at 360, 420 and 670 cm^{-1} due to N or Ga vacancies, also can be observed in ion–implanted GaN samples. The hydrogen–decorated defects can be inspected at 2000 – 2200 cm^{-1}, and Mg–N–H mode represented as electrically inactive complex can be located at 3123 cm^{-1}. Figure 2.11 shows the intrinsic and ion–implanted GaN with LVMs spectrum. In sum-

mary, LVMs can be used to identify point defects in intrinsic and ion–implanted GaN, for the mobility of acceptors, and the evidence of p–type conductivity of GaN.

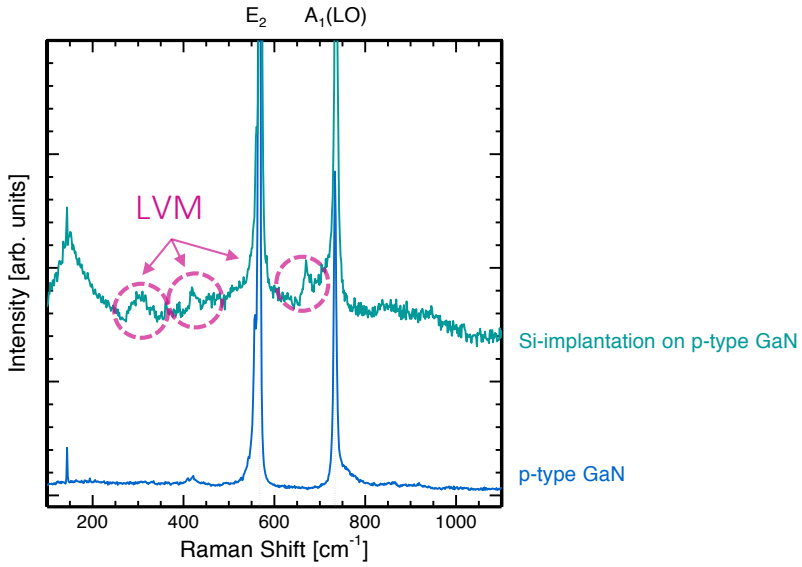

Figure 2.11: Typical Raman spectra of Mg–doped GaN (blue) and Si–implanted on p–type GaN (turquoise) samples. Pink arrows show the defect–induced modes for potential Ga or N vacancies

CHAPTER 3

STUDIES OF INGAAS

3.1 Introduction

$In_{.53}Ga_{.47}As$ is a ternary semiconductor with a zincblende crystal structure. This composition balances the high electron mobility of InAs and the wide bandgap of GaAs. Processing plays a significant role in device realization with controlled n–type and p–type doping. Ion–implantation can help to incorporate dopants into semiconductors with good spatial resolution. Consequently, dopants need to be thermally annealed to repair the crystalline damage and move the dopants into active lattice sites. Lind [57] reported a limit of activation behavior for ion–implanted silicon dopants in InGaAs of $\approx 1.4 \times 10^{19}$ cm^{-3} using rapid thermal annealing method. Sorg [17] reported the feasibility of activating dopants of ion–implanted InGaAs using short-timescale, high–temperature CO_2 or the diode laser anneals. On the other hand, limitation of dopant activation and damage created in the samples has also been investigated using this approach. An activated carrier concentration of 7.6×10^{18} cm^{-3} can be accessed using CO_2 scan at 1 ms dwell for a configuration of 300 nm thin films of $In_{0.53}Ga_{0.47}As$ grown on an InAlAs buffer layer on lattice–matched, heavily doped InP substrates. The dopant activation was observed at 110°C below the damage ($\approx$ 1070 °C), and the highest active carrier concentration was found 30 °C below the damage. We further investigate the activation behavior of a 20 nm Si–implanted InGaAs samples based on this foundation.

3.2 Methods

3.2.1 Samples

Samples, 6 mm by 6 mm in size, consisted of 20 nm intrinsic $In_{0.53}Ga_{0.47}As$ layer grown on a 50 nm InAlAs buffer layer, which was itself grown on a lattice matched, semi–insulating InP substrates with a p–type doping concentration of 10^{18} cm^{-3} (Figure 3.1). One of the samples was capped with a 3 nm Al_2O_3 layer to prevent arsenic evaporation at high temperatures.

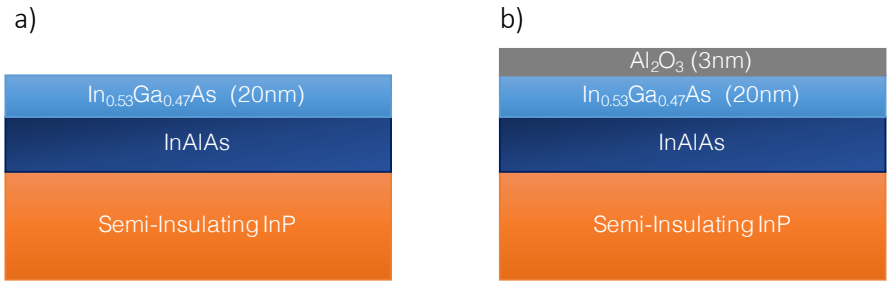

Figure 3.1: Schematic cross-section of Si–doped InGaAs (a) uncapped and (b) capped samples from IBM

3.2.2 Laser Spike Annealing

Laser coupling requires free electrons for absorption. The photon energy of a 10.6 μm CO_2 laser (0.12 eV) is lower than the bandgap of InGaAs (0.75 eV), and hence photons are not absorbed by InGaAs nor InP. Experiments with CO_2 based LSA confirmed no annealing. Based on these findings, we used the 980 nm diode laser (1.3 eV) with a 5 ms dwell to anneal both capped and uncapped InGaAs samples.

To estimate temperatures during LSA, we used the polymer decomposition techniques based on measuring the thickness loss of block copolymer poly(styrene–block–methylmethacrylate), 70 wt.% polystyrene, or as PS–PMMA. After spinning PS–PMMA in toluene on all the InGaAs samples at a rate of 4000 RPM, ramp rate 2000 RPM/s, and at a spin time of 30 seconds, the thickness of the film was measured to range from 57 – 61 nm using a Rudolph FTM ellipsometer and a FilMetrics system (F50-EXR). After LSA on these samples, the change in thickness of the polymer was initially explored using a profilometry system. The change in thickness as a function of position was converted to a function of temperature using relationships established for Si in our lab. In this way, the estimated annealing temperatures of a diode laser with 5 ms dwell was calibrated based on these results.

Thermal calibrations of capped and uncapped InGaAs samples are shown in Figure 3.2 (a). A peak temperature of 1060 °C was estimated for this sample based on the width of the polymer decomposition. Previous results also indicate a damage threshold under CO_2 annealing near 1064 °C [58]. The capped sample reached slightly higher temperature than the uncapped one, resulting in damage. This probably occurred due to thin film interference which increased the optical coupling of the diode laser. Estimated temperature as a function of position for the capped InGaAs samples is also shown in Figure 3.2 (b). The carrier activation was measured by Raman over an 1100 mm width (– 600 to + 500 mm), corresponding to a range of activation temperatures from 900 °C to 1060 °C. We directly estimated the annealed temperature based on the degradation effect, and thus measured the dopant activation that occurred within the region of polymer full decomposition.

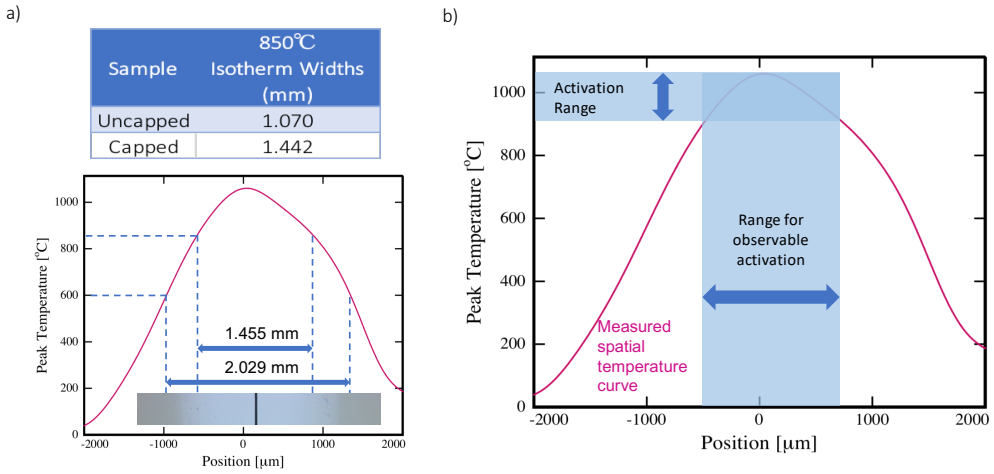

Figure 3.2: Thermal calibration of polymer decomposition based on the spatial temperature profile for InGaAs (a) Isotherm widths of capped and uncapped samples (b) Estimated temperature as a function of the dopant activation regime

3.2.3 Shadow Mask Design and Fabrication

The capped InGaAs sample, which had previously been CO_2 annealed, was annealed with the diode laser at 73 A, 5 ms dwell time to explore the process window before damaging. However, the sample cracked near the exposure line at an estimated peak temperature of only ≈ 880 °C, were below conditions previously used. A higher temperature was anticipated to induce the sample fracture. During LSA, a slightly thinner polymer film (33 nm compared to previous 57–61 nm) was used, and it should act less effectively as an anti–reflective coating, resulting in a lower temperature. The absence of activation also suggests a lower temperature which is consistent with the assumption. Therefore, the mechanism of sample cracking could be thermal shock during opening the shutter for the laser ”on” the sample.

To achieve thermal uniformity during LSA, we developed two 4 by 4 inches

stencil shadow masks with millimeter scale patterns. Figure 3.3 shows the design layout of the two shadow masks, where the first configuration is used for a bottom mask to reduce the laser–induced thermal stress, and the second configuration is used for a top mask to reach thermal uniformity during LSA. Both stencil shadow masks were implemented in the experiment with beam over–scanning, but the top mask was destructively burned due to the high laser intensity. Therefore, a better candidate in replacement of stencil shadow mask was required to survive the laser exposure.

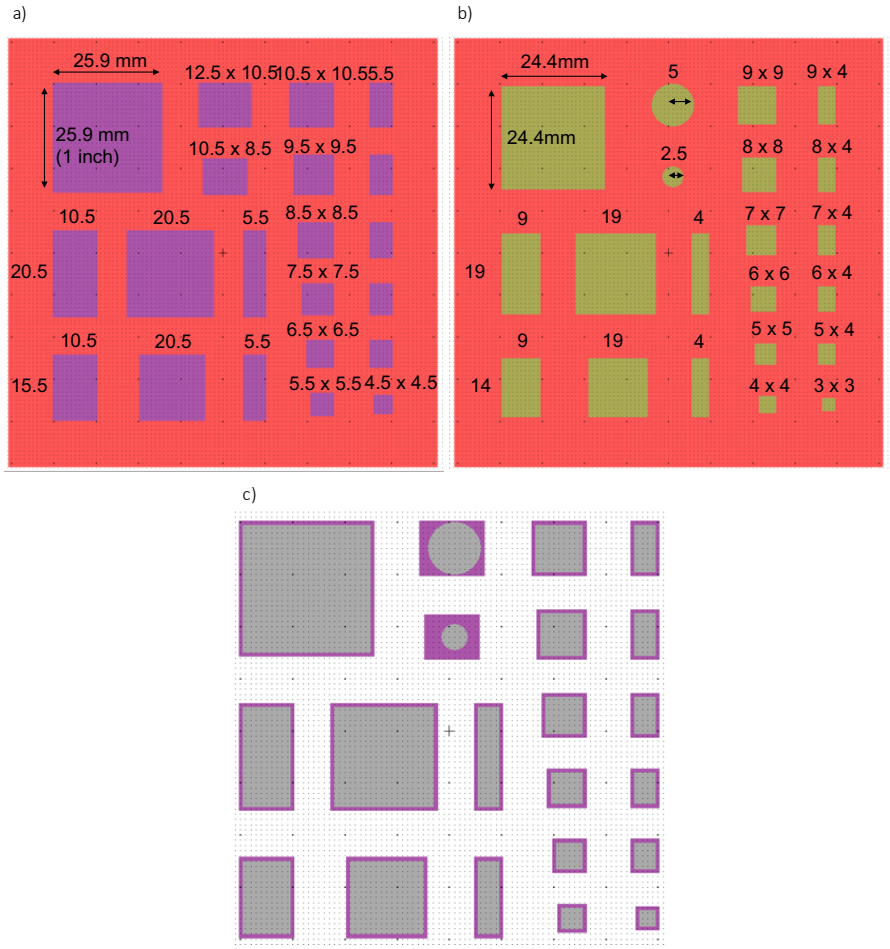

Figure 3.3: Schematic of shadow mask design layout using L–edit CAD

To reduce the thermal shock and achieve thermal uniformity during LSA,

we developed two 4 inches Si–based shadow mask wafers based on the previous stencil templates. Intrinsic silicon plays a better role than the stainless steel due to the optical absorption by phonon coupling rather than free electrons. Therefore, the laser scanning on the sample can provide a uniform optical coupling. The fabrication instructions for the Si–based shadow mask that was used for laser annealing are shown below and in Figure 3.4:

- Spin Shipley 1813 positive tone photoresist on a silicon nitride coated wafer after cleaning
- Expose with 365 nm mid UV source on ABM high resolution mask contact aligner
- Use AZ MIF 726 water developer to remove exposed sections
- Use RIE to remove the nitride membrane (CHF_3 / O_2)
- Remove remaining photoresist with 1165 microposit remover
- Etch using KOH hot bath
- Use RIE to remove both sides of nitride and thermal oxide layers

Silicon nitride is the preferred mask material (as little as 25 nm is sufficient for masking (100) etch all the way through a wafer). We used positive photoresist with photolithography and developed the patterns. Then we etched away the nitride membrane using reactive ion–etching (RIE). Microposit remover and KOH were used to etch away the photoresist and silicon wafer from the mask slots. Finally, RIE was used to remove remained nitride and oxide layers to obtain both shadow masks shown in Figure 3.5.

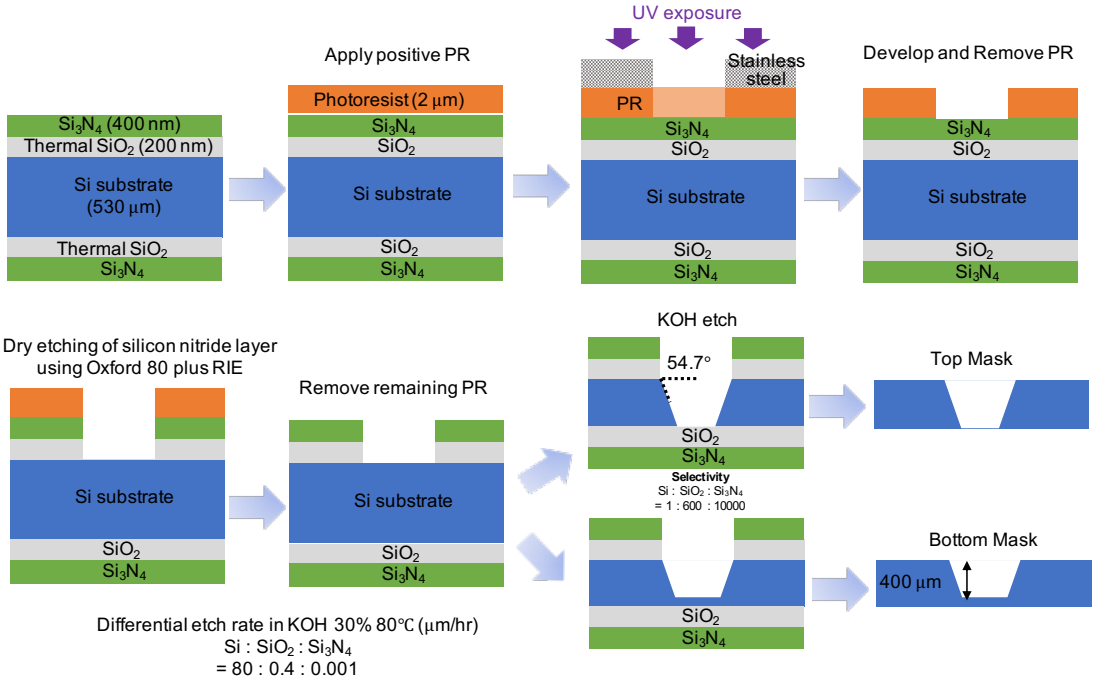

Figure 3.4: Schematic of process flow in Si–based shadow mask fabrication

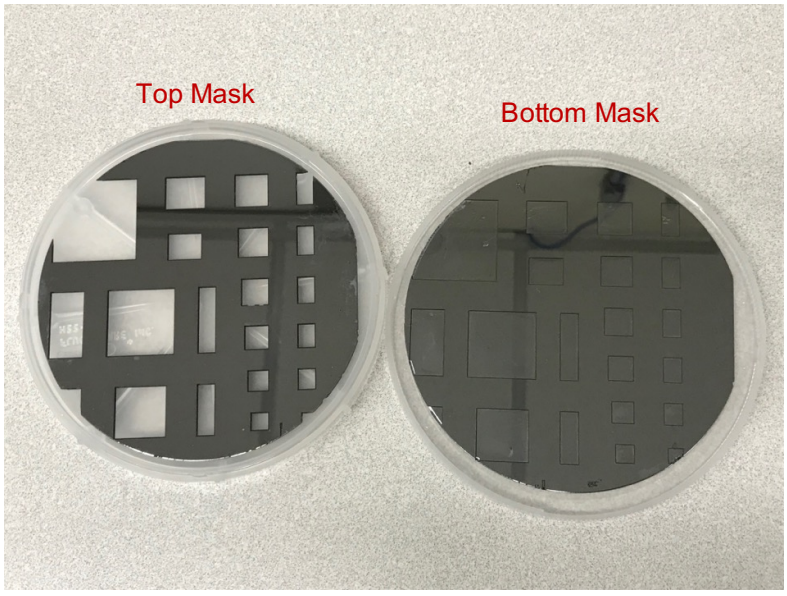

Figure 3.5: Si–based shadow mask wafers

3.3 Results

3.3.1 Laser Spike Annealing of Si–implanted InGaAs

Uncapped InGaAs

Figure 3.6 (a) shows a bright field micrograph of an uncapped, annealed Si–doped InGaAs sample . There was no smoke, nor crack during the annealing process, but a small white flash was observed. From previous studies, this white flash is likely from the laser contacting the copper tape protecting the sample edges. There were also bubbles on the edge of the polymer decomposition section as in the capped sample, but there were fewer visible bubbles in the uncapped sample. No visible damage was found on the annealed sample surface. The annealed peak temperatures almost reached the full polymer decomposition temperature but further data analysis is needed to determine the extent of polymer decomposition.

Capped InGaAs

Figure 3.6 (b) shows a bright field micrograph of a capped, Si–doped InGaAs sample annealed just above the damage threshold, at 75 A laser power. The damage is observed at the center of the sample splitting the sample into two rectangular halves. The variation of color from polymer decomposition section indicates the coupling of diode laser and InGaAs layer, and shows that the sample approached the temperature of the polymer decomposition (600°C to 850°C). The grey lines and patterns on the right side of the sample are more

a)

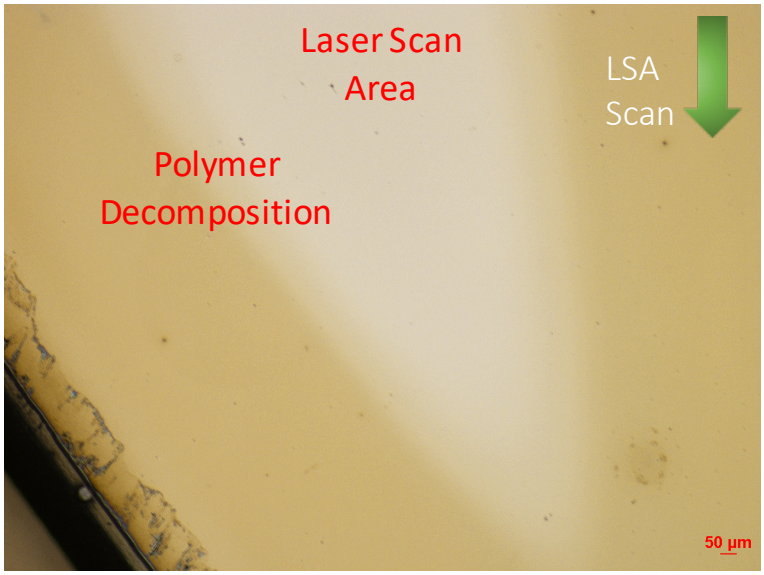

b)

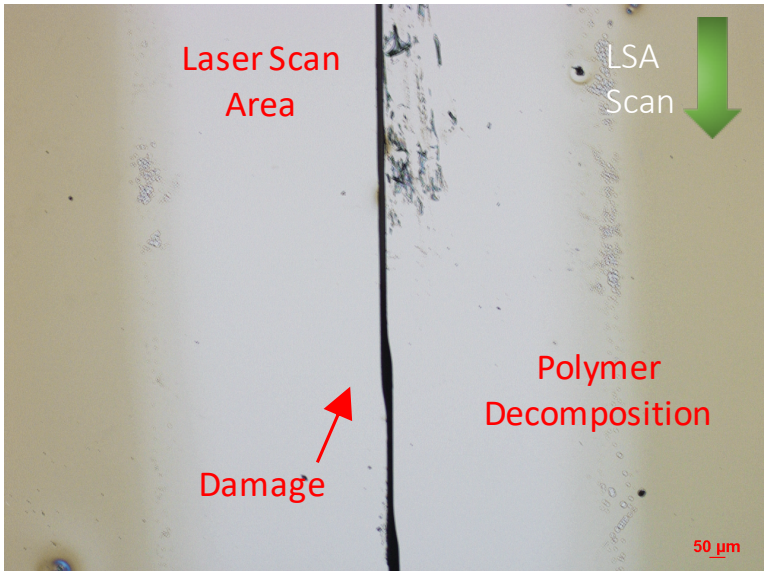

Figure 3.6: Micrographs of the InGaAs sample after diode laser annealing at 75 A, 5 ms dwell time (a) uncapped and (b) capped samples

indicative of scratches from tweezers or removal of copper tape used to protect sample edges, and are not laser damage on the sample. There are small bubbles formed at the edge of decomposition, and the coated area could indicate the start of damage to the sample.

3.3.2 Raman Characterization of Si–implanted InGaAs

Uncapped InGaAs

Raman spectra of capped and uncapped InGaAs samples were collected across laser scans that extended into the damage regime. The LOPCM peak area and peak position were used to estimate active carrier concentrations, as a function of the peak annealing temperature. For the uncapped sample in Figure 3.7 (a), significant carrier concentration could only be activated by sufficient energy at the annealed temperature from $\approx$ 900 °C to $\approx$ 1060 °C. The LOPCM peak continued to rise with increasing temperature, and a statistically significant LOPCM peak was observed with increasing laser intensity. For the analysis of measurable activation, the LOPCM peak occurred at $\approx 1010\ \text{cm}^{-1}$ corresponds to an active carrier concentration of $8.4 \times 10^{18}\ \text{cm}^{-3}$, as shown in Figure 3.7 (b).

Capped InGaAs

For the capped sample in Figure 3.8 (a), the carrier concentration was also observed at the similar annealing temperature. The LOPCM peak escalated abruptly with increasing temperature, and Si dopants began to activate until reaching the damage threshold where the LOPCM peaks collapsed. Fig-

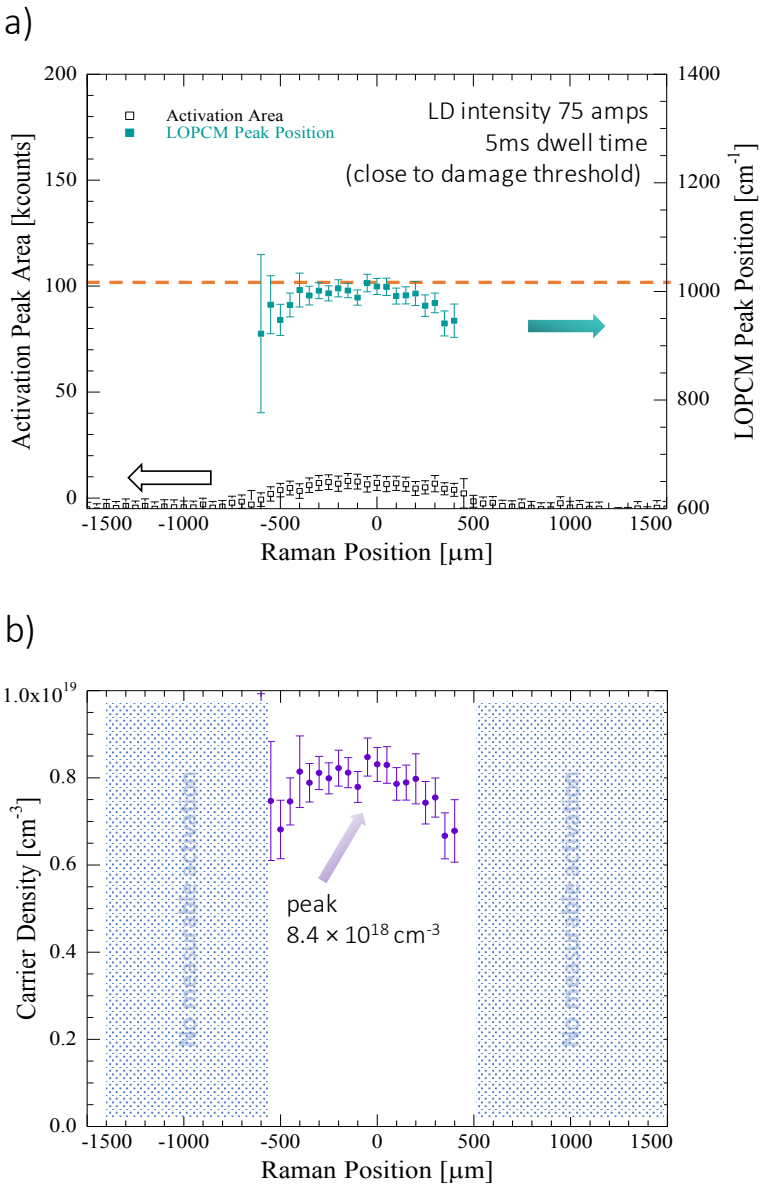

Figure 3.7: Uncapped InGaAs (a) Area and position of the LOPCM peaks (b) LOPCM peak position as a function of carrier density

ure 3.8 (b) showed the LOPCM peak occurred at ≈ 970 cm^{-1} corresponding to an active carrier concentration of 7.8×10^{18} cm^{-3}.

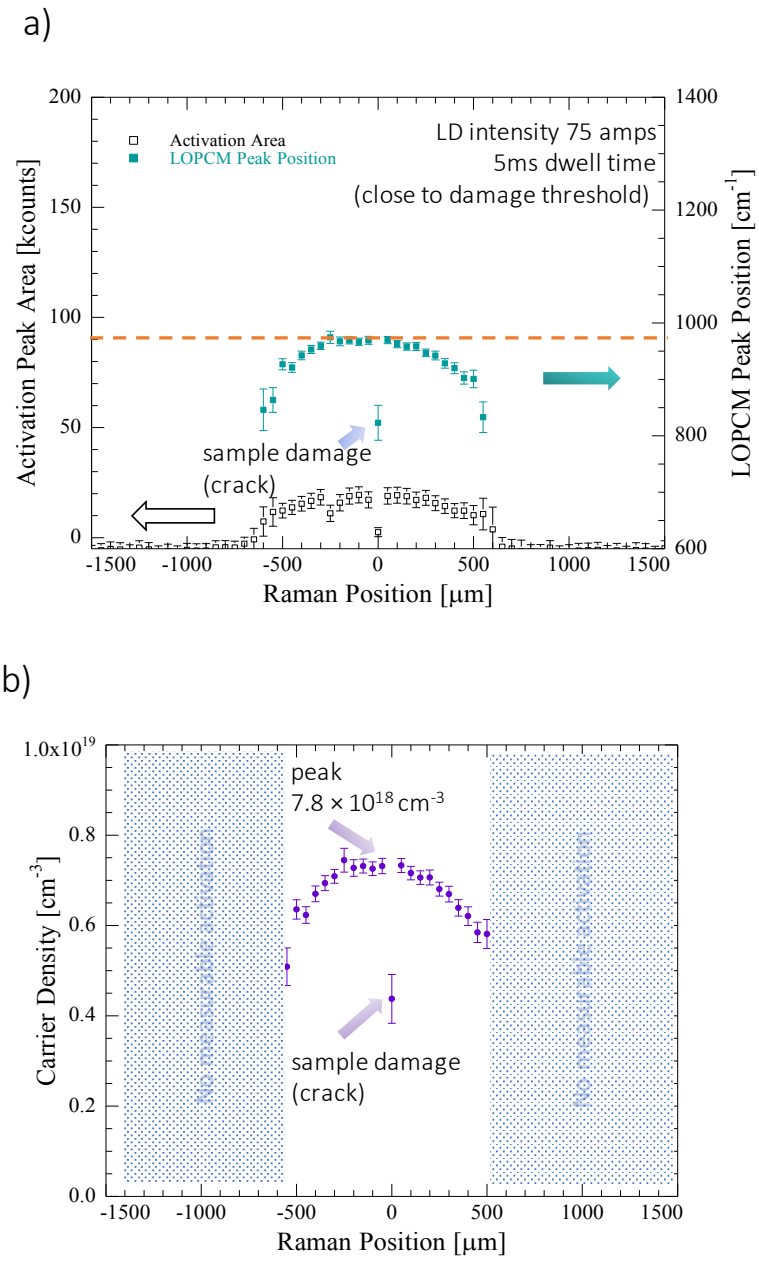

Figure 3.8: Capped InGaAs (a) Area and position of the LOPCM peaks (b) LOPCM peak position as a function of carrier density

3.4 Laser Spike Annealing of RTA annealed InGaAs

An InGaAs samples, with previously activated dopants by RTA, was laser diode annealed at 73 A for a 5 ms dwell. The intent of this experiment was to determine if LSA could improve the activation further. Samples were annealed at 73 A with 5 ms dwell on InGaAs surface area of 5 by 5 mm^2 using the Si–based shadow mask approach. The sample still fractured after annealing at these conditions, despite a thermal isotherm width of $\approx 980\,\mu$m and an estimated peak temperature of ≈ 960 °C. Figure 3.9 shows the Raman spectra of pre and post–laser annealed samples. The carrier concentration of 9×10^{18} cm^{-3} for pre and post–annealed, based on the converted LOPCM peak positions, indicating a maximum dopant activation of Si implantation and damage limitation in RTA–processed InGaAs sample, as shown in Figure 3.10. No significant change in the dopant activation was observed. Equally, however, no deactivation was observed.

3.4.1 Potential Mechanism for Damage Onset

Challenges remain for dopant activation in capped samples during annealing. The sample cracking may be the results of hot spots in the laser itself. Laser intensity variation and intrinsic instability in InGaAs absorption can impact the actual laser beam on the sample surface. Therefore, an identification of inhomogeneities in laser diode beam was required. The profile of laser beam at sample plane must be calibrated to directly observe the potential hot spot in laser intensity. Indeed, the polymer decomposition width as a function of laser power may also need to be calibrated in a dense volume. The effect of thermal "runaways",

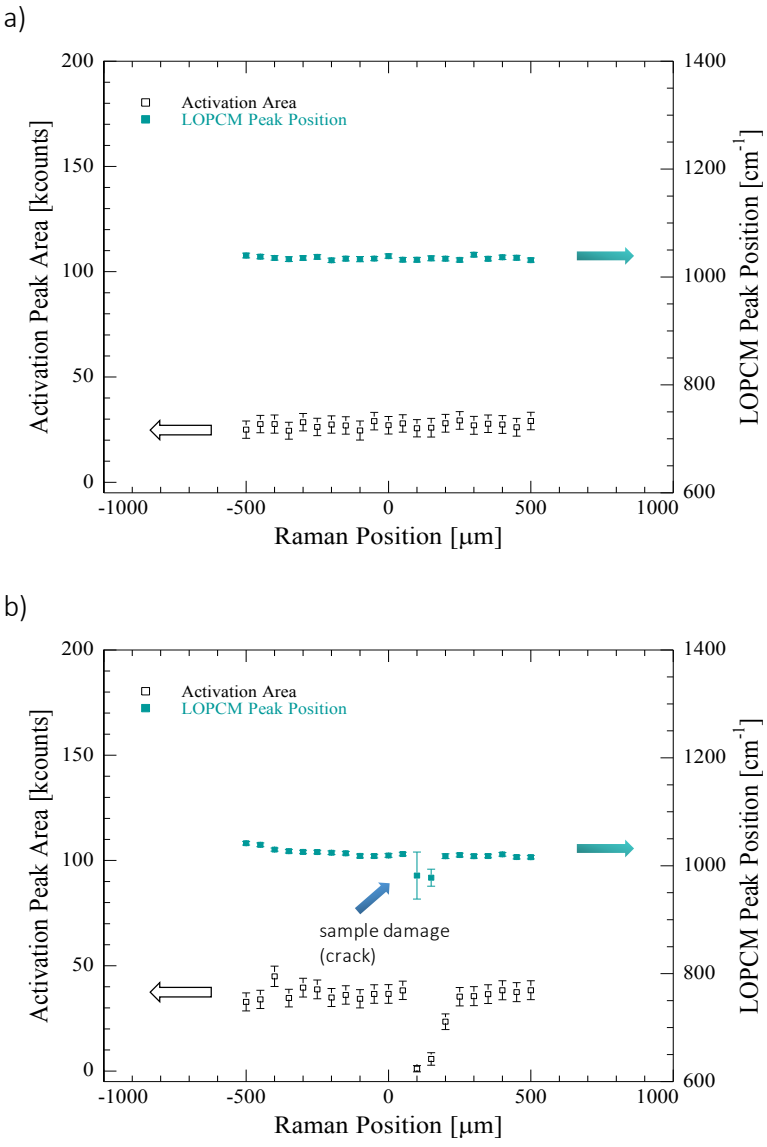

Figure 3.9: Raman spectra of LOPCM area and peak position for (a) pre–anneal (b) post–anneal RTA processed InGaAs sample.

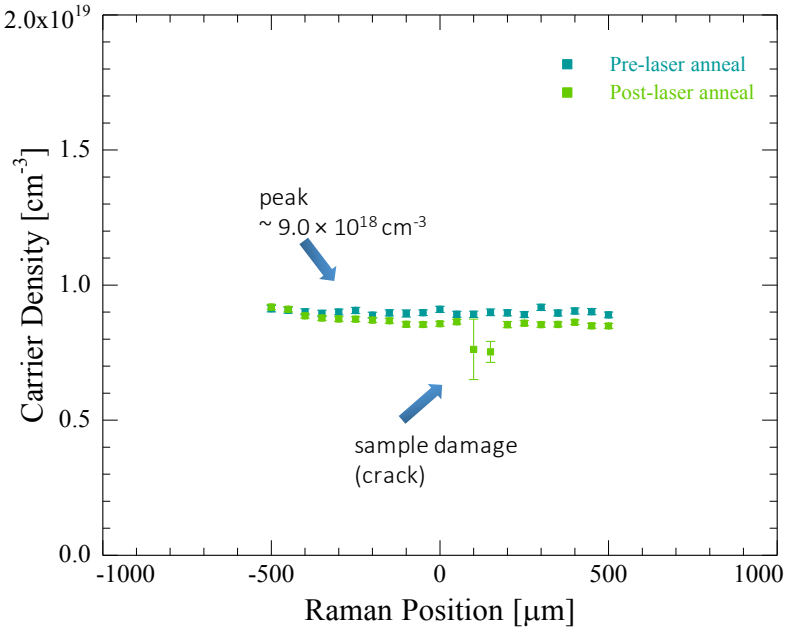

Figure 3.10: Carrier concentration of RTA processed InGaAs sample for pre and post–laser anneal on 73 A, 5ms dwell time

due to the high adsorption and a sudden spike in temperature, might resulted from the non–homogeneities laser beam. Fabricating oxide layers on the InGaAs surface, to absorb a CO_2 wavelength, may reduce the abrupt temperature rise.

3.5 Summary

The feasibility of annealing 20 nm Si–implanted InGaAs junctions was studied using laser spike annealing. Both uncapped and the capped InGaAs samples successfully coupled with the 980 nm diode laser at 75 A, 5 ms dwell, and reached temperatures above the onset of polymer decomposition ~ 650 °C. A range of activation temperatures from 900 °C to the damage threshold at a peak temperature at 1060 °C was estimated, corresponding to the carrier activation

measured by Raman. Based on the LOPCM analysis, active carrier concentrations for both capped and uncapped InGaAs samples reached 80% of the implanted dose during laser diode LSA.

To determine if LSA could improve the activation, LSA on RTA InGaAs samples using 980 nm diode laser at 73 A, 5 ms was studied. Si–based shadow mask wafers were developed to reduce the thermal shock and achieve thermal uniformity during LSA. No activation and deactivation behaviors were observed, and the estimated peak temperature at the damage threshold was 960 °C. Challenges still remain for dopant activation in capped samples during annealing, and possible solutions such as hot spots identification and design consideration for a heated stage to reduce thermal shock during annealing may be necessary in the future.

Appendix – CO_2 LSA on Capped InGaAs

As mentioned in the introduction, CO_2 annealing of these samples was unsuccessful. Figure 3.11 shows the results of annealing with increasing laser powers. A visible white flash for 24 and 40 W annealing was observed, and the coated polymer only decomposed at the end of stripes as the beam left the sample. The non–uniform polymer decomposition indicated that a steady state was never achieved, but was expected to be achieved within a few mm of the sample edge. This indicates the CO_2 laser does not couple with InGaAs thin film layers on undoped InP substrate due to an insufficient free electron for optical absorption.

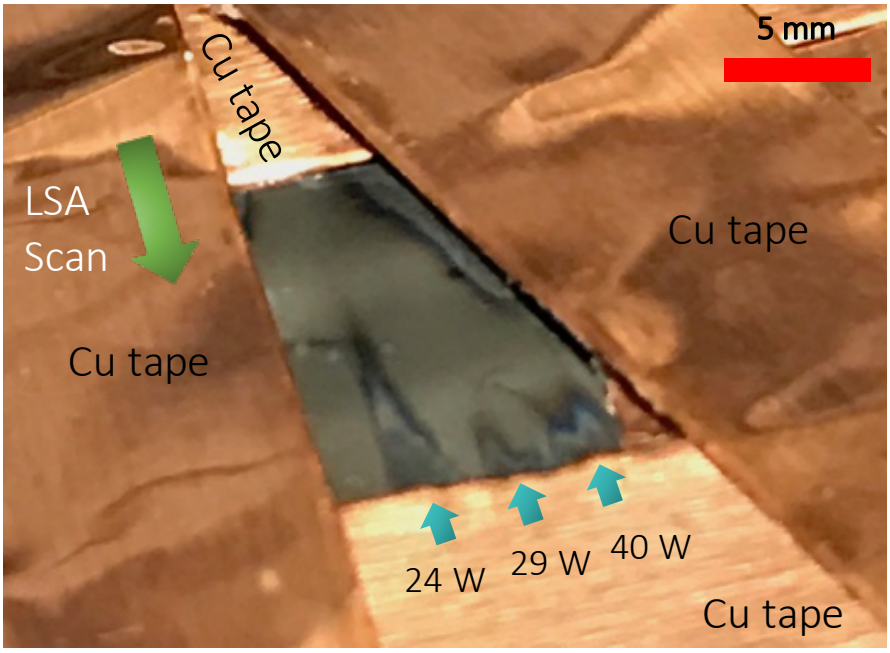

Figure 3.11: CO_2 LSA on capped InGaAs with laser intensity from 24 to 40 watts

CHAPTER 4

STUDIES OF GAN

4.1 Motivation

Gallium Nitride (GaN) exhibits both high carrier mobility and high breakdown voltage, characteristics that are essential for power and high voltage applications. As in all semiconductor materials, device performance relies on controlling p– and n–type doping levels. However, dopant activation of selective Si implantation on as–grown p–type GaN for the application of vertical power device remains challenging. In this chapter, we used confocal Raman microscopy with depth profiling technique to probe different heterogeneous GaN structures to characterize free carrier density. We further investigated the effects of LSA on Si-doped and p-doped GaN with Fermi–level calculations for point defect formation verification.

4.2 Samples

Wurtzite-structured GaN samples used in this study were provided by our collaborators in the Jena and Xing research groups at Cornell. The samples were up to 1 by 1 cm^2 in size. Initial tests for laser annealing were conducted, determining that CO_2 laser annealing was feasible for this material. Six general sample types were used as shown in Figure 4.1. Bare substrates were obtained from two suppliers, Hitachi and Sunitoro (Fig. 4.1a), with both exhibiting similar levels of defects. Epitaxial GaN layers with well–controlled defects were

grown on substrate of sapphire or GaN from Hitachi. For GaN substrates, the defect levels in the substrate were too high to fabricate high quality devices, and the lower defect, the GaN epilayer is critical. Four different epitaxial carrier concentrations for 7 μm n–type film were studied (Fig. 4.1 b); the implant concentrations are in the range of 2×10^{16} cm^{-3} to 6.5×10^{17} cm^{-3}. Two epitaxial carrier concentrations for 400 nm Mg-doped p–type film on top of n–type epitaxial GaN, grown on Hitachi substrates, were studied (Fig. 4.1 c,d). The implant concentrations were 1×10^{19} cm^{-3}. Two Si–implanted carrier concentrations for 400 nm n–type film on top of the previous devices were studied (Fig. 4.1 e,f), with implants to 1×10^{19} cm^{-3}. For the Si–implanted devices, dopant concentrations were estimated by stopping and range of ions in matter (SRIM) shown in Figure 4.2. For all the samples except R4281, a ≈80 nm PECVD silicon nitride (Si_3N_4) capping layer was added to prevent nitrogen evaporation during high–temperature annealing. Samples were annealed using CO_2 based LSA with 1 ms dwell, and for peak temperatures up to 1500 °C, and then studied to understand the dopant activation behaviors of Si-doped GaN devices.

4.3 Raman Depth Profiling

Confocal Raman spectroscopy was used to probe carrier densities as a function of depth for annealed samples shown in Figure 4.3. This depth profiling was used to analyze features at specific layers below the sample surface and provide structural information. A blue laser at 488 nm was used for the Raman measurements, with a penetration depth ≈ 1 μm of GaN based on Eqn. 3.2. With the laser focused on the surface of the GaN sample, the microscope stage scans in the vertical direction changing the illuminated volume. In this

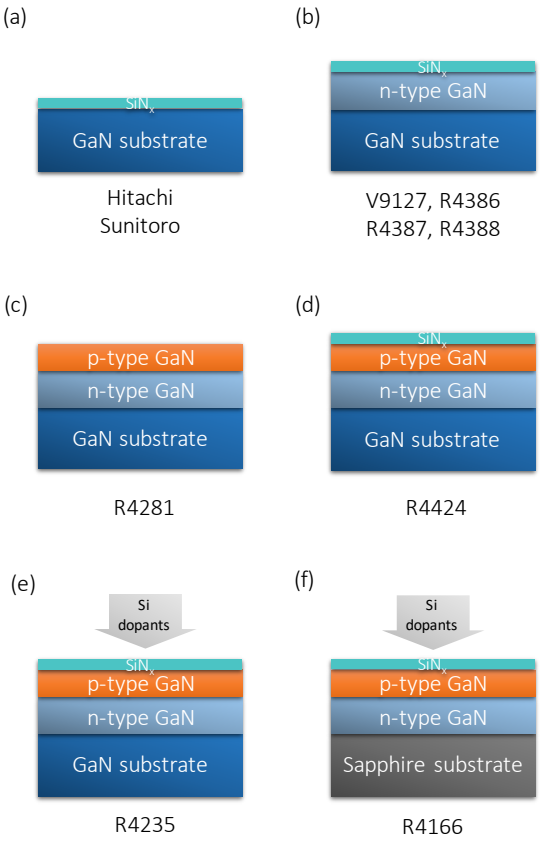

Figure 4.1: Cross-sectional view of the GaN samples (a) Sunitoro and Hitachi substrates (b) R4386, R4387, R4388, and V9127 are epitaxial n–type layer on Hitachi substrate (c) R4281 is epitaxial Mg-doped p–type layer on top of n–type GaN grown on Hitachi substrate (d) R4424 is identical to R4281 device and capped with Si_3N_4 layer (e) R4235 is Si implanted on top of previous p–type GaN device and capped with Si_3N_4 layer (f) R4166 is Si implanted on top of previous p–type GaN device grown on a sapphire substrate

Si ion implantation into
p⁺-GaN 20nm/ p-GaN 400nm
Target dose concentration: 1E19/cm^3

1. 30keV, 1.2E13/cm^2
2. 50keV, 2.0E13/cm^2
3. 100keV, 4.8E13/cm^2
4. 180keV, 8.4E13/cm^2
5. 280keV, 1.8E14/cm^2

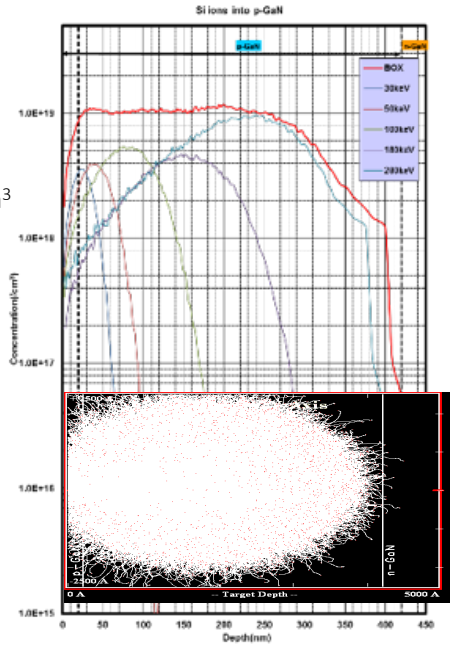

Figure 4.2: Schematic of stopping and range of ions in matter (SRIM) simulation of Si atom doping into p-GaN material. Reproduced with permissions from Nomoto et al.

way, complex samples and multilayer structures in GaN could be readily characterized. Raman spectra for the two substrates and epitaxial n–type films with varying carrier concentration were measured both at low and high frequency. The low frequency shift ranges from 150 to 400 cm^{-1}, and high frequency shift ranges from 700 to 900 cm^{-1}. The layered structures of GaN devices could be determined based on this foundation and was calibrated further.

Carrier Densities in Intrinsic GaN

The bulk GaN substrates (Hitachi and Sunitoro) were measured as shown in Figure 4.4 (a). In the case of Hitachi substrate, the L^+ peaks of 751 cm^{-1} and L^- peaks of 163 cm^{-1} suggested a corresponding carrier concentration at $\approx 6.5 \times 10^{17}$ cm^{-3}. In the case of Sunitoro substrate, the L^+ peaks of 857 cm^{-1} and L^-

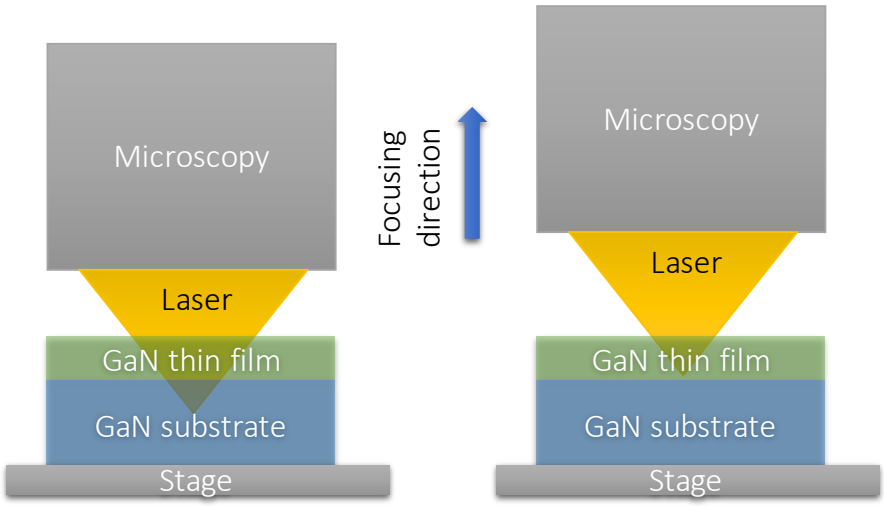

Figure 4.3: Laser beam path focused at the GaN substrate and microscope stage scanned in a vertical direction to the surface of thin films

peaks of 379 cm^{-1} suggested a corresponding carrier concentration at $\approx 4.8 \times 10^{18}$ cm^{-3} shown in Figure 4.4 (b).

Carrier Densities in n–type GaN

Raman measurements on the surface and at depth in various n–type GaN are shown in Figure 4.5 (a). Using depth profiling, the difference of doping level in the n–type epitaxial films was clearly distinguished as shown in Figure 4.5 (b). In the case of three types of GaN device, the L^+ peaks of 733 cm^{-1} and unclear L^- peaks suggested a low concentration level at the top layer of devices. The estimated carrier concentrations was 10^{16} – 10^{17} cm^{-3}, but was too low to be accurately determined However, as focusing into the sample of 9 μm, the L^+ and L^- peaks suggested a corresponding carrier concentration at $\approx 2 \times 10^{18}$ cm^{-3} in the bulk, which was referred to the doping level of bulk GaN substrate. Therefore, the investigation of the carrier concentration of n–type GaN can be

a)

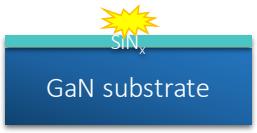

Hitachi
Sunitoro

b)

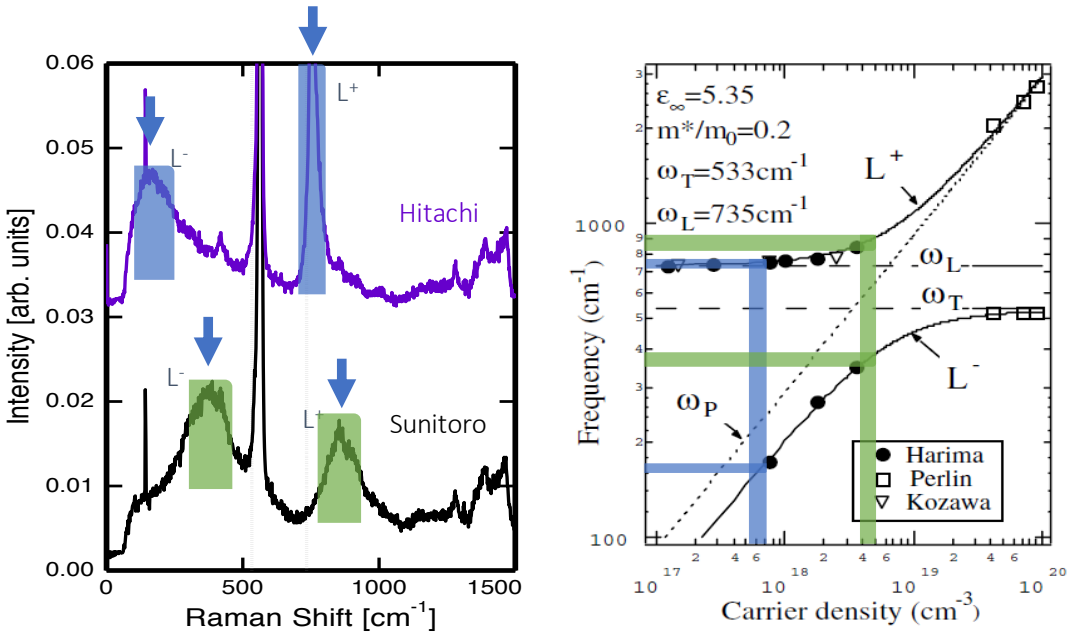

Figure 4.4: (a) The schematic of Raman measurement on the surface of both intrinsic GaN samples (b) Raman spectra taken in single acquisition for both both bulk GaN substrates. The colored arrows in (a) identify the coupled peak positions and their corresponding carrier density is highlighted in (b)

carried out successfully using depth profiling.

a)

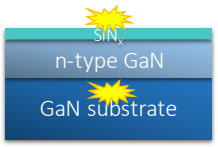

V9127, R4386, R4387

b)

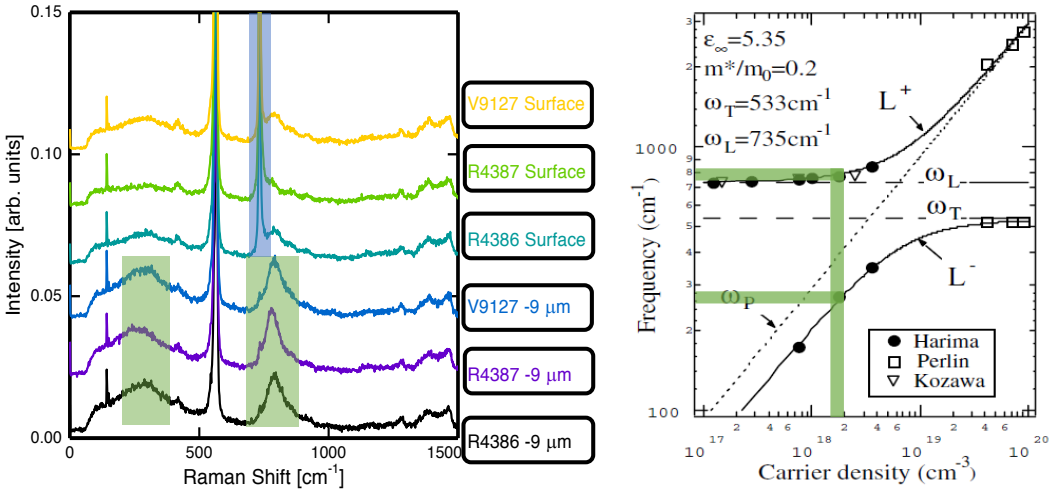

Figure 4.5: (a) The schematic of Raman measurement on the surface of doped GaN samples (b) Raman spectra taken in single acquisition for different depth of layers in GaN samples. Top three curves presented as the surface of doped GaN and the bottom three curves showed bulk substrates. The colored arrows in (a) identify the coupled peak positions and their corresponding carrier density is highlighted in (b)

Carrier Densities in p–type GaN

Carrier concentration of p–type GaN was investigated as shown in Figure 4.6. There is no peaks corresponded to the L^+ and L^- in p-doped GaN and thus the hole concentration cannot be determined. Otherwise, the results were

identical to the n–type GaN measurements. The carrier concentration in the GaN substrate was $\approx 1.8 \times 10^{18}$ cm^{-3} as determined by depth profiling.

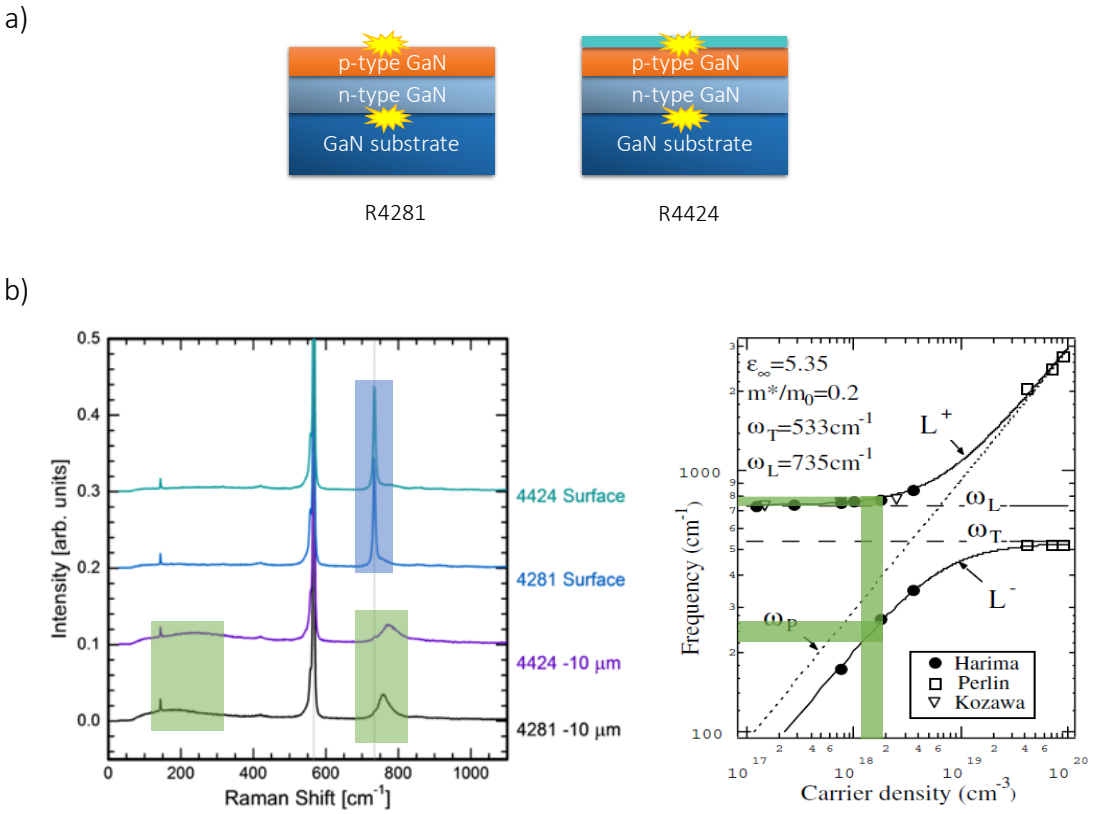

Figure 4.6: (a) The schematic of Raman measurement on the surface of p-doped GaN samples (b) Raman spectra taken in single acquisition for different depth of layers in GaN samples. The colored arrows in (a) identify the coupled peak positions and their corresponding carrier density is highlighted in (b)

4.3.1 Carrier Densities in Si-implanted GaN after CO_2 LSA

Dopant activation on both GaN on GaN and GaN on sapphire using laser spike annealing are shown in Figure 4.7 and 4.8. The carrier shifts in L^+ and L^- peak indicated the concentration exceeded the 1×10^{19} Si/cm^{-3} implanted

dose with up to 2×10^{19} carriers/cm^{-3}. The implant was correctly measured reaching the activation peak temperatures, and the increased carriers might be thermodynamically favored charge vacancies [48] or an extrinsic dopant from the capping layer during high laser temperature annealing. Further investigation is needed.

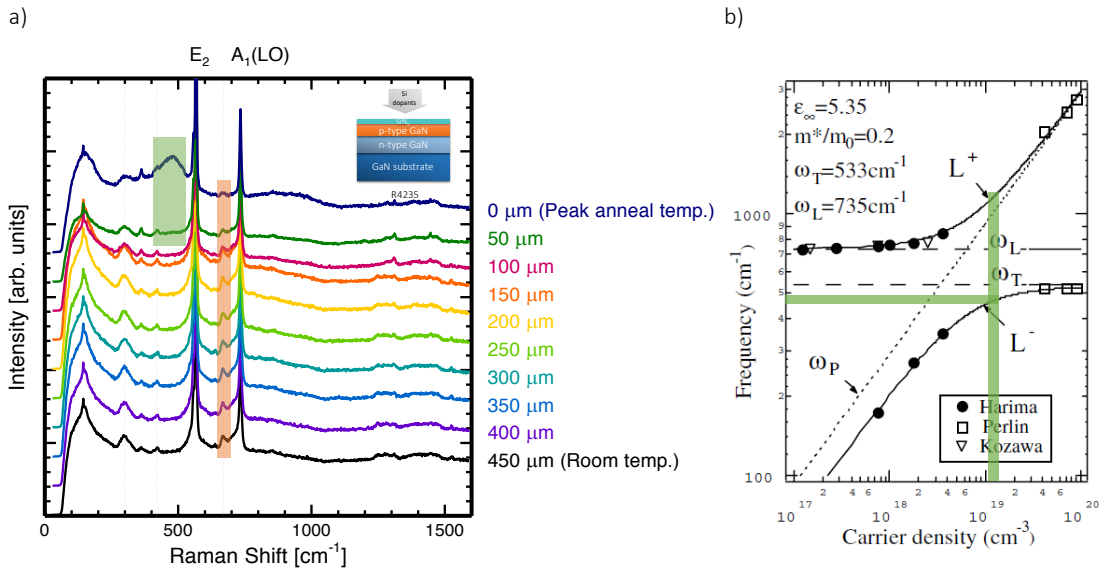

Figure 4.7: GaN on GaN : The Raman spectra taken from the left side of the annealing stripe (a) and the calibration for converting peak position to carrier concentration (b). Moving up the plots, the spectra are taken closer to the laser stripes, the bottom black line being unannealed. The colored arrows in (a) identify the coupled peak positions and their corresponding carrier density is highlighted in (b). The coupled peaks show that the sample exhibits dopant activation, with carrier concentrations in the 1 $\times 10^{19}$ cm^{-3} to 2 $\times 10^{19}$ cm^{-3} range

4.3.2 Discussion : Defect formation energies of doping in GaN

To determine the carrier densities responsible for n–type conductivity, a computational investigation was conducted to determine defect and impurity

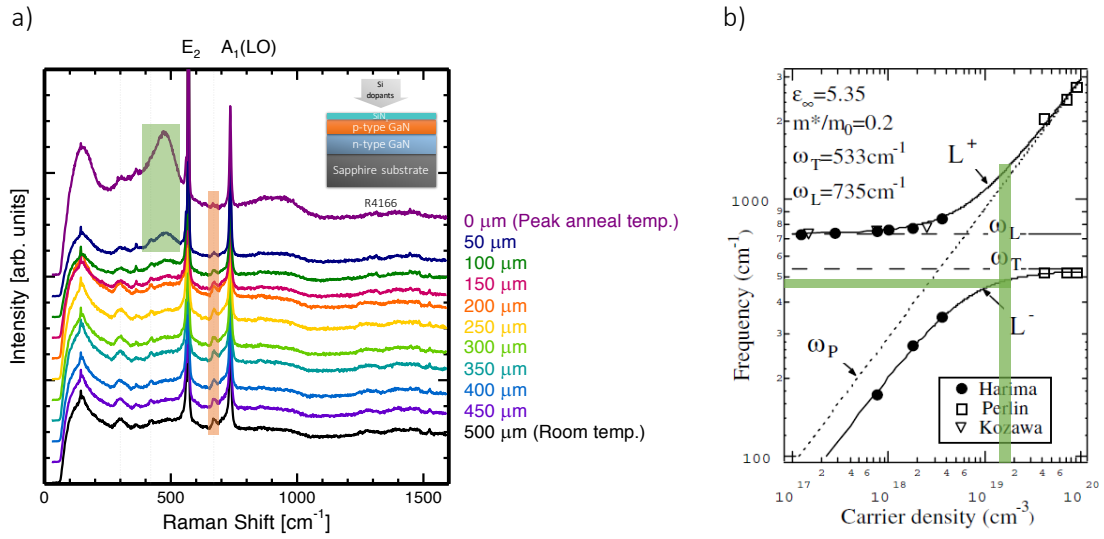

Figure 4.8: GaN on sapphire : The Raman spectra taken from the left side of the annealing stripe (a) and the calibration for converting peak position to carrier concentration (b). Moving up the plots, the spectra are taken closer to the laser stripe, the bottom black line being unannealed. The colored arrows in (a) identify the coupled peak positions and their corresponding carrier density is highlighted in (b). The coupled peaks show that the sample exhibits dopant activation, with carrier concentrations in the 1 $\times 10^{19}$ cm^{-3} to 2 $\times 10^{19}$ cm^{-3} range

concentrations based on first-principles formation energies [59]. First-principles calculations for native point defects in GaN [60, 61, 62], as well as impurities ion–implanted [63, 64, 65, 66] have previously been reported. In the case of n–type doping, the oxygen (O_N) and silicon (Si_{Ga}) dopants act as shallow donors, which can be readily incorporated with relatively low formation energies in n–type GaN. In contrast, the nitrogen vacancies (V_N) unlikely to occur in significant concentrations due to the high formation energies, as shown in Figure 4.9. In the case of p–type doping, magnesium (Mg) is selected as the acceptor dopant for hole concentration but potentially limited by other n–type impurities [67, 68]. V_N has lower formation energy in a p–type material which could act

as a compensating center and increase the electron concentration [69]. Hydrogen also has substantial effects on the passivation of acceptors during growth [70, 71]. H behaves as a donor (H^+) in p–type GaN to compensates acceptors but behaves as an acceptor (H^-) in n–type GaN. Therefore, laser annealing on p–type GaN for both capped and un-capped samples enable the verification of the V_N acting as a donor in p–type GaN.

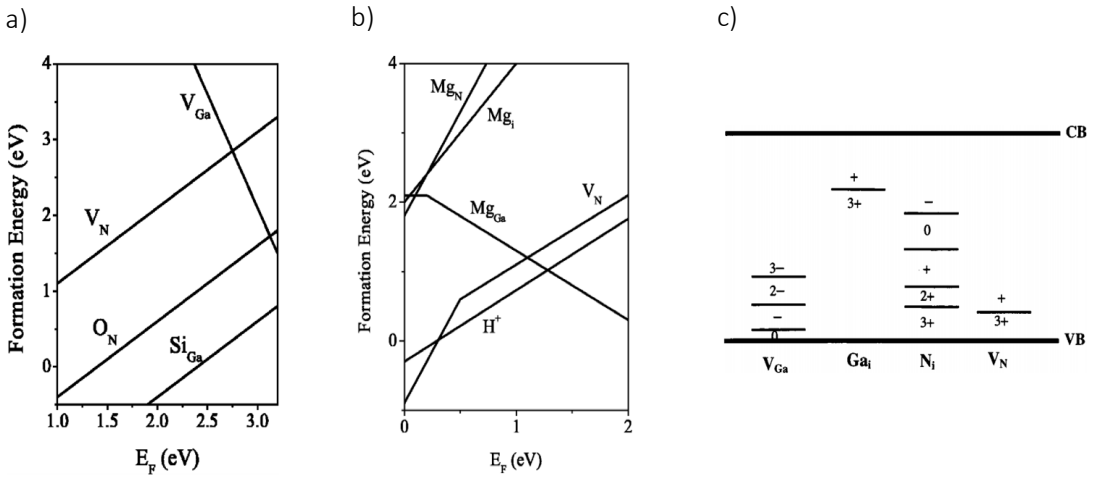

Figure 4.9: (a) Formation energy as a function of Fermi level for native defects (nitrogen and gallium vacancies) and donors (oxygen and silicon) in n–type GaN. The zero of Fermi energy is located at the top of the valence band. (b) Formation energy as a function of Fermi level for native defect (V_N), interstitial H, Ga-substitutional, N-substitutional, and interstitial configurations. Gallium-rich conditions and equilibrium with GaN and Si_3N_4 are assumed in both cases. (c) Thermal transition states for defects in GaN were determined by the calculation of defect formation energies. Reproduced with permission from Van De Walle and Neugebauer, copyright Journal of Applied Physics 2004

4.4 Summary

The feasibility of depth profiling of GaN devices using confocal Raman microscopy in short timescale and high temperature CO_2 LSA was demonstrated. Carrier concentrations of GaN substrates, thin films, and epitaxial GaN layer grown on GaN and sapphire substrates were identified. Dopant activation of Si–implanted samples during LSA was measured by Raman, and carrier density exceeded by two times the implant concentration. Further investigation on these results is needed.

CHAPTER 5

FULL-FIELD THERMOREFLECTANCE SPECTROSCOPY

5.1 Introduction and Motivation

A recent advance in high–throughput characterization of thermal processing is the lateral-gradient laser spike annealing (lgLSA) technique, which has drawn particular interest to identify meta–stable phases that can develop on sub-millisecond timescales. This technique has also been used in this work for III–V compound material investigations [17].

One of the key challenges in lgLSA is accurate temperature measurements across the beam profiles, and measurements of the temporal profile to determine thermal heating and quenching rates. Previous work measured temperatures during lgLSA in the sub-millisecond time regime using a resistance–based temperature detector, with extensive absolute calibration to block copolymer and Au melt, coupled with simulation modeling. These methods are inherently slow, complex and difficult. Thus, full field in–situ measurement during lgLSA has been established [31].

There are various potential thermal measurement approaches, including non–contact optical techniques such as Raman spectroscopy [72], photoluminescence [73, 74], and thermoreflectance [75]. Thermoreflectance, in particular, can be used as a powerful tool to determine the temperatures and establish heat transfer properties. Measurements have been implemented in MEMS and microfluidic devices applications, and current thermoreflectance imaging techniques are capable of measuring thermal performance and thermal properties

in novel microscale and nanoscale electronic, optoelectronic, photonic, and thermoelectric devices and materials.

At its simplest, thermoreflectance is based on the change in reflectivity of a material surface with temperature at a chosen wavelength. Thermoreflectance imaging of semiconductor devices has been investigated by several groups using various probing sources and wavelengths. Tessier et al. measured Au and NiCr coated with Si_3N_4 on a GaAs substrate using a Ti:sapphire laser with 240 nm as a UV source. The calibrated thermoreflectance coefficient, defined as $\kappa = \left(\frac{1}{R}\frac{\partial R}{\partial T}\right)$, was reported to be $3 \pm 0.5 \times 10^{-5}$ K^{-1} [53].

Further measurements were conducted using immersion lenses at $\lambda = 1.7\,\mu$m with values of 5.2×10^{-4} in Si and 2.2×10^{-3} on the Au resistance was obtained [76]. A review of thermoreflectance coefficients for metals and semiconductor materials used for thin film electronics in visible wavelengths and specific temperature regions have been established recently [77], and have been used to investigate thermal properties of devices such as quantum cascade lasers and VECSELs (vertical external-cavity surface-emitting lasers) [78, 79].

In this work, we developed and implemented an in-house charge-coupled device (CCD) thermoreflectance (CCD–TR) spectroscopy to determine the full 2D thermal field during lgLSA [40]. We demonstrated this complementary strategy to profile the temperature field of CO_2 laser spike annealing with both spacial and temporal profiling. The measurements can be simultaneously coupled with imaging of black–body radiation at high temperature. We compare CCD–TR results with Pt thermistor and simulated data over dwell time from 250 μs to 2 ms, demonstrating that the thermal images can be quantified for the full field temperature profiling during LSA.

5.2 Design and Concepts

The principle of thermoreflectance imaging is based on the temperature dependence of the surface reflectivity of materials corresponding to changes in the refractive index. Given a room temperature reflectivity R_0 and a change in reflectivity ΔR, the reflectivity can be linearlized in the temperature change ΔT as

$$\frac{\Delta R}{R} = \left(\frac{1}{R}\frac{\partial R}{\partial T}\right)\Delta T = \kappa \Delta T \tag{5.1}$$

where κ is the thermoreflectance coefficient (typically on the order of 10^{-6}–10^{-4} K^{-1} for metals and semiconductor materials). To determine ΔT, a monochromatic probing light with intensity I is illuminated on the inspected surface and the reflected light I' is measured with a CCD camera, which allows determination the local temperature at each pixel using the equation:

$$\Delta T = \kappa^{-1}\frac{\Delta R}{R} = \kappa^{-1}\left(\frac{I' - I}{I}\right) \tag{5.2}$$

5.2.1 Selection of Illumination Wavelength

To accurately measure the temperature of the material surface, calibration of the thermoreflectance coefficient (κ) is critical. However, published data regarding the dependence of κ on temperature is limited and difficult to predict; in addition, the reflectance of material is dominated by the optical absorption, interactions of phonon and carrier, electronic bands and transitions, polarization

and other factors. Therefore, κ might vary nonlinearly over a broad temperature range.

Silicon, as the most widely used semiconductor, is well studied and accurate knowledge of the optical functions of silicon at elevated temperatures exist [80]. The reflectance (R) of Si at normal incidence can be determined using the equation:

$$R = \frac{(n_1 - n_2)^2 + k^2}{(n_1 + n_2)^2 + k^2} \tag{5.3}$$

where n is the refractive index and k is the extinction coefficient. At other angle with unpolarized light, the Fresnel equations with s and p polarizations must be used:

$$R_s = \left|\frac{n_1 \cos\theta_i - n_2 \cos\theta_t}{n_1 \cos\theta_i + n_2 \cos\theta_t}\right|^2 = \left|\frac{n_1 \cos\theta_i - n_2 \sqrt{1 - \frac{n_1}{n_2}\sin\theta_i}}{n_1 \cos\theta_i + n_2 \sqrt{1 - \frac{n_1}{n_2}\sin\theta_i}}\right|^2 \tag{5.4}$$

$$R_p = \left|\frac{n_1 \cos\theta_t - n_2 \cos\theta_i}{n_1 \cos\theta_t + n_2 \cos\theta_i}\right|^2 = \left|\frac{n_1 \sqrt{1 - \frac{n_1}{n_2}\sin\theta_i} - n_2 \cos\theta_i}{n_1 \sqrt{1 - \frac{n_1}{n_2}\sin\theta_i} + n_2 \cos\theta_i}\right|^2 \tag{5.5}$$

where n_1 is refractive index of the incident medium, n_2 is refractive index of the refracted medium, θ_i is the incident angle, and θ_t is the refracted angle. For 45° incidence light, the average reflectivity is just the average as indicated by Equation 5.7.

$$R = \frac{R_s + R_p}{2} \tag{5.6}$$

Figure 5.1 shows normal incidence reflectance of Si at visible wavelengths for a number of elevated temperatures [81]. Near the direct band–gap, the reflectivity changes rapidly with temperature. Between 420 and 600 nm, the variation is smooth; 470 nm gives also a high absorption coefficient with surface sensitivity. Blue LED can be used as sources in this wavelength range.

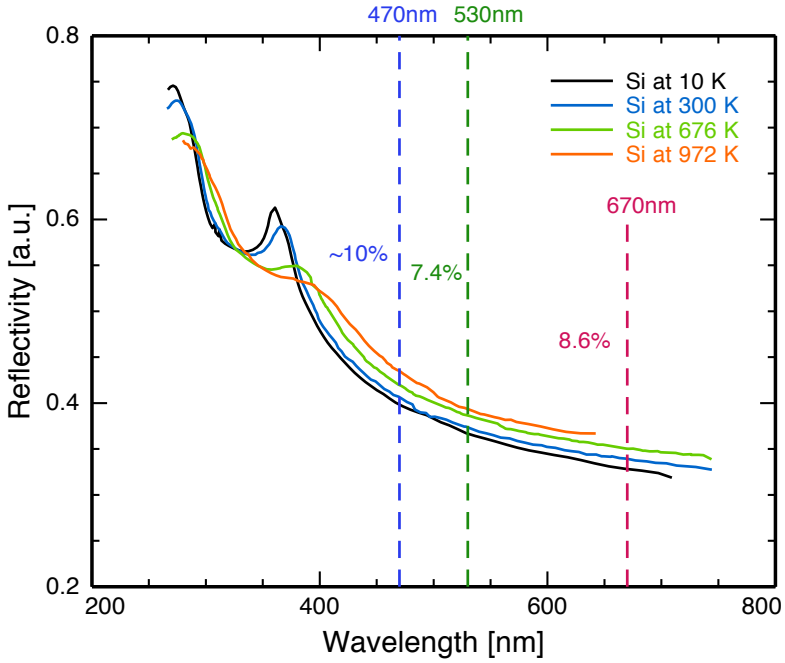

Figure 5.1: Reflectivity of Si as a function of wavelength at various temperatures

The setup of CCD thermoreflectance integrated with the lgLSA system is shown in Figure 5.2. The surface of the device is illuminated by a 470 nm light emitting diode (LED) (Lumex). The reflectance at an angle of ~ 45 degrees was captured through a long working distance microscope (Navitar), connected to a 12-bit CCD camera (Teledyne DALSA). The exposure time of the CCD measurement was set at 3 ms to minimize the thermal noise in the camera. The area

of interest for the CCD camera was chosen as 1280 x 1024 pixels in a Bayer image resolution. CCD thermoreflectance provides faster surface mapping with a higher signal-to-noise ratio (SNR) and time resolution than a photodetector, and LED-based probing system can also avoid the issue of interference fringes and illumination drifts during image acquisition [82].

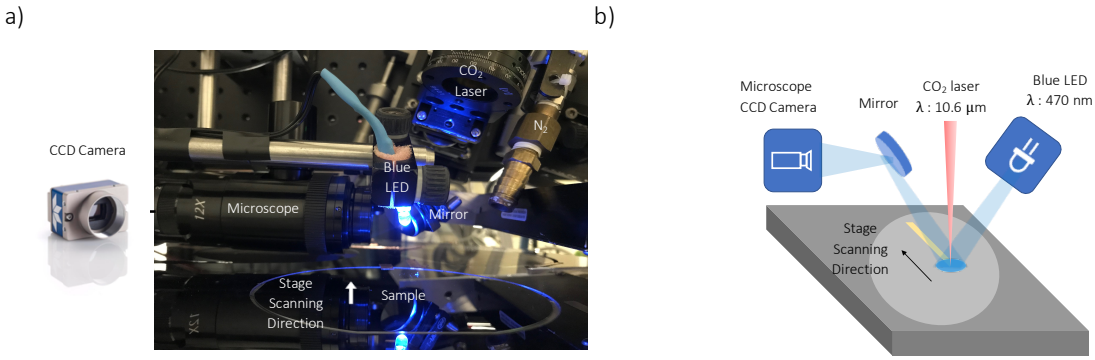

Figure 5.2: (a) Integration of thermoreflectance imaging with laser spike annealing system at Cornell (b) Schematic of the thermoreflectance imaging system. An LED illuminates the device, and the reflected light is detected through the mirror by the CCD camera. The incident CO_2 laser beam couples with sample surface at near normal incidence

The determination of κ is critical for accurate temperature measurements and depends on material properties [46], wavelength of illuminating light [76], surface roughness, numerical aperture (NA) of objective [83], angle of incidence, and composition for multilayer structures [40, 84]. The 470 nm LED used in this work was selected based on the indirect bandgap of Si and highest absorption coefficient to remain surface sensitive. The reflectivity of the heavily B–doped Si substrate (ρ= 0.01 – 0.02 Ω·cm) is expected to match closely to the temperature dependent optical properties of nominally undoped Si reported by Jellison [81].

To perform thermoreflectance imaging, a line-focused continuous wave CO_2 laser (λ = 10.6 μm, 250 W) was used as the irradiation source on the lgLSA sys-

tem. The laser was focused with crossed cylindrical lenses to a width of 88 μm in the scan direction and a transverse width of 508 μm, with both axes having Gaussian distributions in intensity. Annealing times and peak temperatures were modulated by adjusting the scan speed and laser power. The dwell time (τ_{dwell}), used to characterize heating durations, is defined as the ratio of the laser intensity full–width–at–half–maximum (FWHM) in the scan direction divided by the scan velocity. In this study, velocities of 40–400 mm/s were used to explore dwells from 250 μs to 2 ms. Prior temperature calibrations based on Au melt and measurements with a Pt thermistor were also used. These calibrations were critical to the interpretation of the spatially resolved properties during laser scanning.

5.3 Image Processing and Noise Analysis

Temperature profiles during LSA were obtained from CCD thermoreflectance images as shown in Figure 5.3. The CCD camera acquired two sets of image stacks for I(T), and I(T_0), where I(T) was taken during the laser scan (at T_{peak}) while the I(T_0) was taken post-scan with the laser off (at T_{room}). The relative reflectance change at each pixel was determined:

$$\frac{\Delta R}{R} = \frac{I(T) - I(T_0)}{I(T_0)} \tag{5.7}$$

To avoid interference from black–body radiation, reflectance changes used only the blue channel of the CCD images. As seen in Figure 5.3 (a), small changes in the raw image become clear temperature profiles in the ΔR/R image. Figure 5.3 (b) details the image processing flow to convert raw CCD images

a)

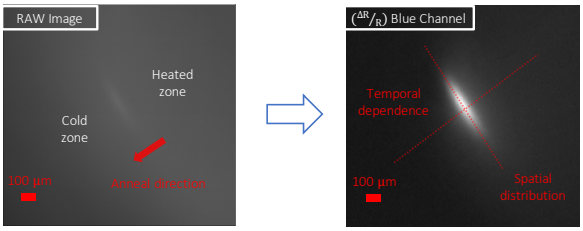

b)

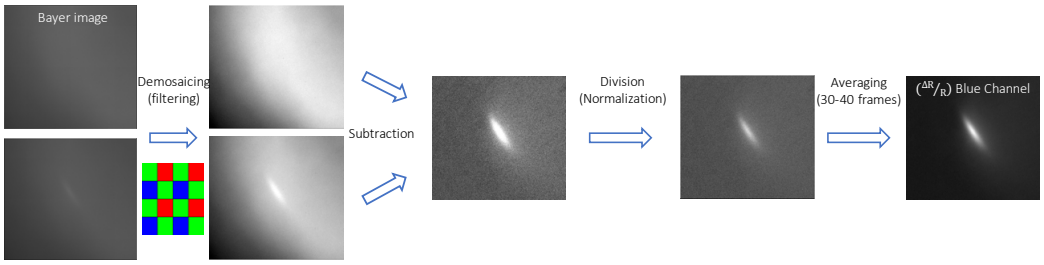

Figure 5.3: (a) Schematic of the principle of thermoreflectance imaging is presented. Reflection was measured as laser irradiating to the device. The differential image between high and low reflectivity presents thermal profiles and variations, and the inset presents the temperature distribution in the spatial and temporal direction (b) Image processing flows for spatial and temporal resolution of $\Delta R/R$ calculation

into the thermal images. Analysis of images used the ImageJ software package (http://imagej.nih.gov/ij). Analysis steps include channel filtering, image normalization, and frame averaging. A conversion from raw CCD Bayer format to a true–color RGB image was first performed, followed by filtering of the blue color only for reflectance. The background image (no laser on LED) was subtracted and the image was then normalized. Frames were then averaged to increase the SNR of thermoreflectance signals, with about 30 to 40 frames used in the averaging. Longer dwell time provide more frames for image acquisition. The spatial size of each pixel was calibrated using a patterned device

wafer yielding 0.556 pixel/μm in the spatial direction (orthogonal to the scan direction), and 0.477 pixel/μm in the scan direction.

5.3.1 Temperature Dependence of Thermoreflectance Response

The maximum reflectivity change $\Delta R/R$ for scans were obtained by fitting the spatial and temporal profiles. These data are plotted as a function of the estimated temperature (previous calibrations) in Figure 5.4. Also shown are previous measurements of the change from static (hot plate) experiments by Jellison [81] and Vuye [85]. The thermoreflectance data are generally consistent with the extrapolation of relative reflectance changes from the spectroscopic rotating polarizer ellipsometer results. These results indicate near-linear behavior with temperature changes with a thermoreflectance coefficient of 1.4×10^{-4} K^{-1}. This is close to the measured valuue of 1.2×10^{-4} K^{-1} from Jellison and Vuye [81, 85]. However, there is clear non–linear behavior above 1200 °C for 470 nm illumination. There are serveral potential causes for this non–linearity including (i) coupled changes in n and k at high temperature, (ii) interference from black-body radiation or (iii) invalid temperature calibrations. Hence, detailed analysis of thermoreflectance at high–temperature in the RGB spectrum was undertaken.

5.3.2 Black–body Detection for High-temperature Region

As temperatures increase above 500°C, black–body radiation (BBR) begins to emit significant amounts of visible light from the material itself based on the Stefan–Boltzmann formula:

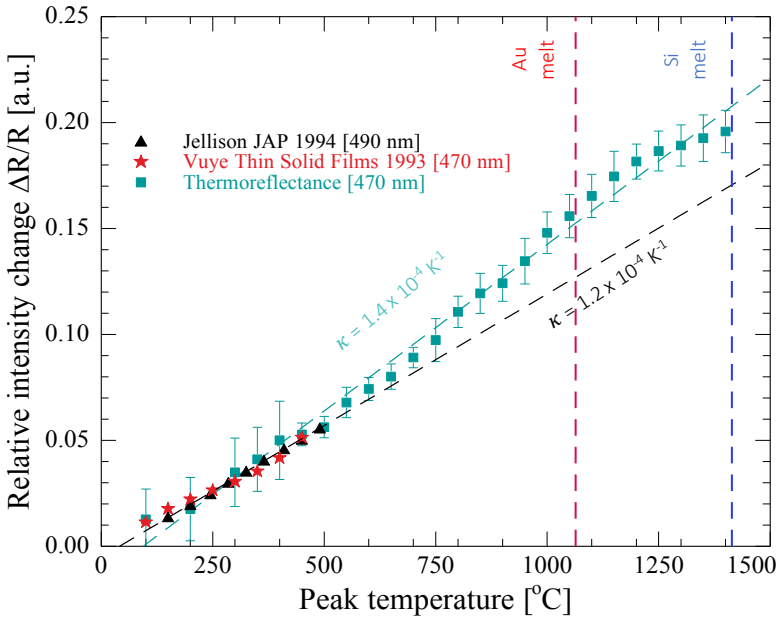

Figure 5.4: Reflectivity as a function of the estimated dashed line as a linear fit to the LSA data with $\kappa = 1.4 \times 10^{-4}$ K^{-1}

$$E = \sigma T^4 \tag{5.8}$$

where E is emission energy flux and σ is Stefan-Boltzmann constant (5.67×10^{-8} $\frac{W}{m^2 \cdot K^4}$). With the LED light off, BBR emission ($\propto T^4$) can be detected for temperatures above 1000°C using the CCD camera. Thermal images can be spit into three RGB channels (red, green and blue) as shown in Figure 5.5 (a), where the blue channel shows almost exclusively reflected LED light, the green channel is mixed LED reflection and BBR, and only BBR was observed in the red channel. Hence, the BBR emission effect is dominant in the red channel, with some signal in green channel, but with almost no impact on the blue channel. Removing these interferences will be useful for accurate thermal signal characterization, and improve thermoreflectance SNR during LSA shown in Figure 5.5 (b).

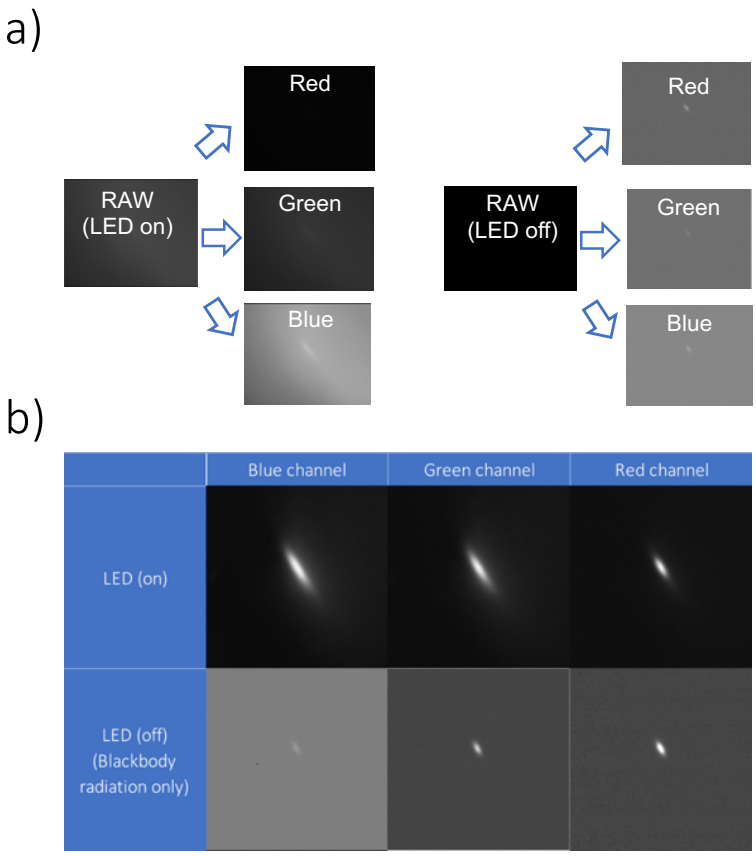

Figure 5.5: Imaging blackbody radiation in blue, green and red channels. The contribution of BBR is negligible in the blue channel, contribute partially in the green channel, and dominates in the red channel

5.4 Results and Discussions

5.4.1 CO_2 Laser Temperature Measurements and Behavior

The peak reflectivity changes $(\Delta R/R)_{max}$ as a function of the estimated peak temperature, obtained from fitting of the spatial and temporal profiles, are shown in Figure 5.6 (a). To confirm temperature calibrations, Au melt and Si melt threshold at 1 ms were identified at 40.15 W (equivalent to T_{melt} at 1064 °C)

and 46.245 W (equivalent to T_{melt} at 1414 °C) which overlaps the calibrated curve as shown in Figure 5.6 (b).

These curves were obtained for a range of dwell times from 250 μs to 2 ms; as shown in Figure 5.6. For all dwells, the curve shapes are very similar, indicating a consistent temperature calibration process. The average thermoreflectance coefficient (κ) over the temperature range from room temperature to 1200 °C is $\cong 1.42 \times 10^{-4}$ K^{-1}, which is in good agreement other measured values of 1.2 – 1.5 $\times 10^{-4}$ K^{-1} (measured over narrower temperature ranges) [81, 86, 87, 88, 89]. The consistency of measured $\Delta R/R$ as a function of the previous calibrated temperatures over the full dwell range suggests the non–linearity is indeed intrinsic to Si and the conversion from $\Delta R/R$ to temperature must use the calibration calculated in Figure 5.6 (c).

5.4.2 Spatial Temperature Profiles

Incident CO_2 laser intensity profiles were obtained by measuring the beam intensities using a pinhole and photodiode. The beam intensity is only a reasonable estimate for the thermal beam dimension and FWHM as temperature profiles and gradients along the lateral direction (along with the long beam axis) depend on thermal diffusion laterally and into the substrate. Thermoreflectance imaging allows measurement of temperatures both orthogonal to the scan direction (lgLSA mode) as well as in the time axis through temperature profiles in the scan directions.

The temperature profile orthogonal to the scan direction of the CO_2 beam on a B–doped Si ($\sim 5 \times 10^{18}$ cm^{-3}) is shown in Figure 5.7 (a). The spatial temperature

a)

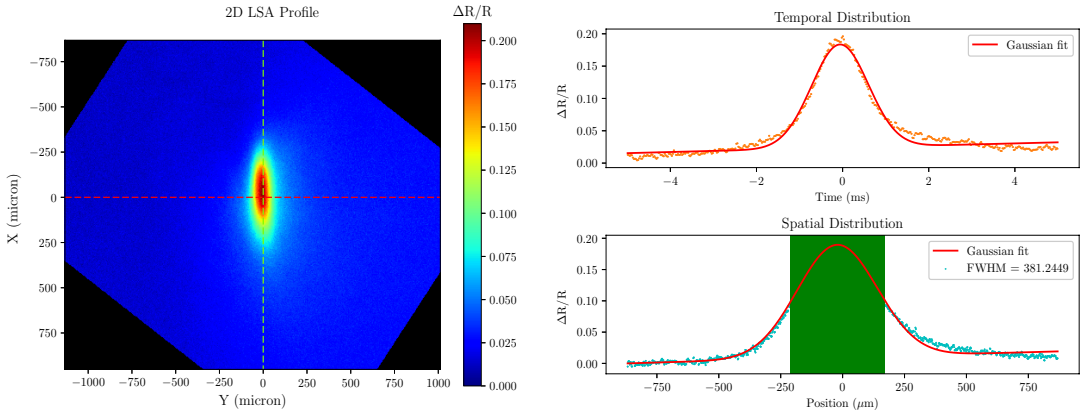

2D LSA profile with Gaussian fitting curves

b)

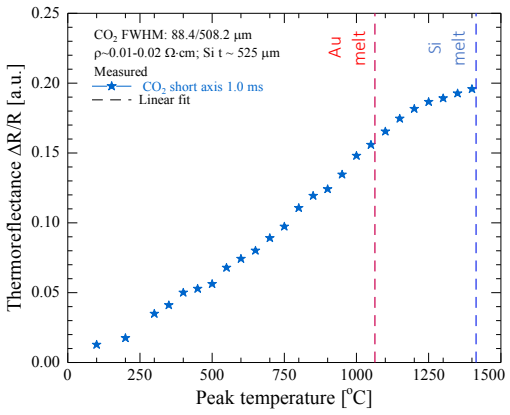

c)

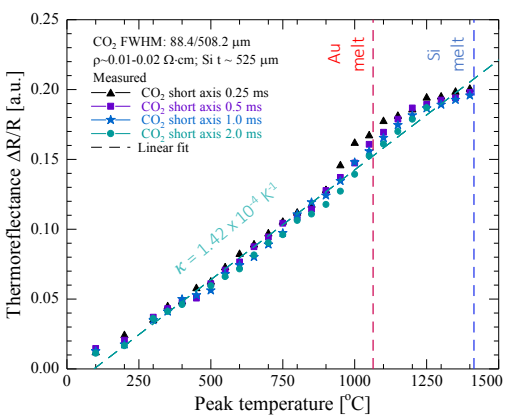

Figure 5.6: Thermoreflectance from CO_2 LSA scans as a function of previous temperature calibrations (a) Fitting of lateral and temporal profiles to determine the peak $\Delta R/R$ (b) Data for a 1 ms dwell with indicated known points for Au and Si melt (c) Overlay of Data with range of dwells from 250 μs to 2 ms

and intensity profiles can be approximated as Gaussians using the function:

$$P_G(x \mid \mu, \sigma) = \frac{1}{\sqrt{2\pi\sigma^2}} \exp\left[-\frac{(x-\mu)^2}{2\sigma^2}\right] \tag{5.9}$$

where μ is the mean and σ is the standard deviation. The Gaussian standard deviation is related to the FWHM through $\sqrt{8\log 2}\sigma \approx 2.355\sigma$. The FWHMs of temperature profiles measured from thermoreflectance were 457 ± 86 m for 1 ms dwell scan, which is significant narrower than the FWHM obtained from intensity profiles of 508.2 μm. As the laser power increases, the thermal conductivity in these regions decreases and the lateral thermal diffusion becomes limited, subsequently making the temperature profile steeper, which results in a smaller FWHM. Together with an increasing scanning velocity (τ_{dwell} decreasing), the thermal dissipation in these regions are also restricted, inducing the steeper thermal profile with the smaller FWHM, as shown in Figure 5.7 (b). The effect is quite significant with FWHM reduced by more than 30% from 400 °C to 1100 °C.

5.4.3 Temporal Temperature Profiles

The temporal profile of the millisecond CO_2 LSA can also be extracted from the thermoreflectance images as shown in Figure 5.8. Distances are converted to equivalent time through the known stage velocity. For a dwell of 500 μs (Fig. 5.8 (a)), the substrate temperature begins to rise ~ 1 ms prior to the peak. After the laser passes through, the substrate begins to cool by thermal conduction into the bulk. Within ~ 4 ms, the temperature drops below ≈ 150°C for all laser powers observed. As the laser power increases, both heating and quenching

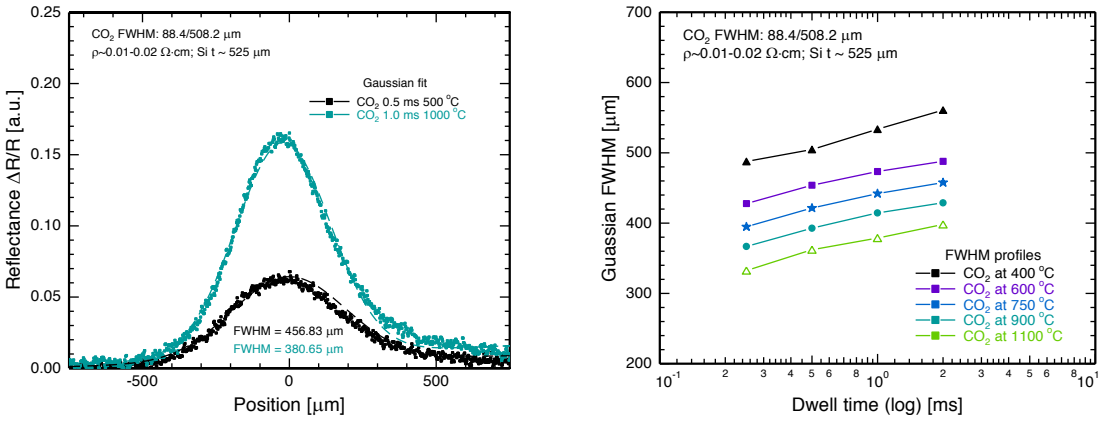

(a) Spatial profile of Si substrate

(b) FWHM comparison at different temperature for τ_{dwell} ranging from 250 to 2000 µs

Figure 5.7: Spatial temperature profiles during CO_2 LSA (a) Spatial profile for 500 μs and 1 ms on Si substrate (b) Comparison of FWHM °C for τ_{dwell} ranging from 0.25 to 2 ms on a logarithmic scale. A smaller FWHM is observed in shorter dwell and at higher temperature due to the impact of thermal diffusion

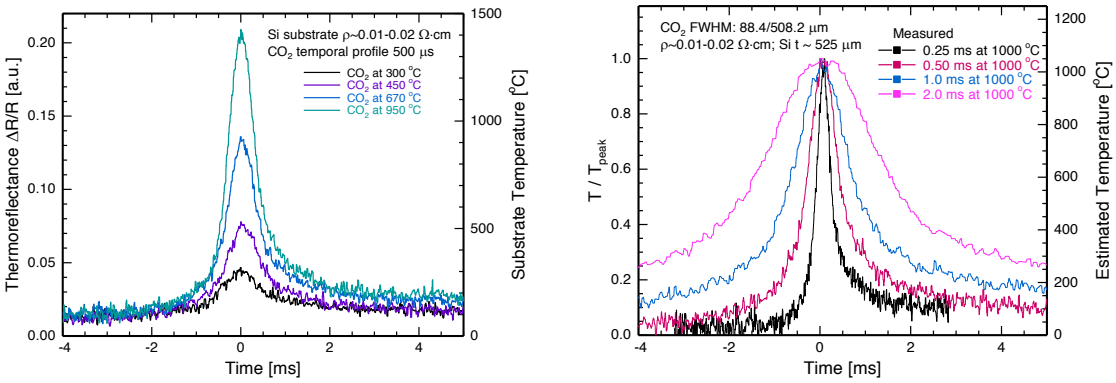

(a) Temporal profile at constant τ_{dwell}

(b) Temporal profile at constant peak temperature

Figure 5.8: Temporal profiles during CO2 LSA (a) T.R as a function of temperature for constant τ_{dwell} at 500 μs (b) τ_{dwell} at constant substrate temperature ($\Delta R/R_{peak}$ obtained from a TR imaging)

rates increase dramatically under these spike annealing behaviors.

The normalized temperature profiles from thermoreflectance for a range of dwells at a constant peak temperature are shown in Figure 5.8 (b). Significant broadening of the profile is observed for increasing τ_{dwell} due to the longer heating duration and thermal diffusion length where L = $\sqrt{4D\tau_{dwell}}$.

5.4.4 Comparison with Pt Thermistor Temperature Profiles

Temperature profiles from thermoreflectance were compared to Pt thermistor measurements. Byungki Jung developed the platinum thin-film resistor method to measure LSA temperature, and utilized them for direct temperature measurements during the millisecond LSA of Si wafer substrates. These resistor devices (referred to as thermistors) have spatial and temporal resolution consistent with measuring temperature profiles. For a single laser scan, the peak resistance change (ΔR_{max}) can be measured over the thermistor device at a given power and τ_{dwell}. The resistance change of Pt film is expected to be directly related to temperature by the following relation:

$$R = R_0(1 + \alpha\Delta T) \tag{5.10}$$

where α is the temperature coefficient of resistance (TCR) for Pt, and R_0 is the resistance at a reference temperature T_0.

The spatial profiles during a 1 ms CO_2 LSA at comparable peak temperatures are shown in Figure 5.9 (a). While both profiles are similar, the FWHM of the thermistor measurement is $\approx$ 100 μm larger than that of the thermoreflectance.

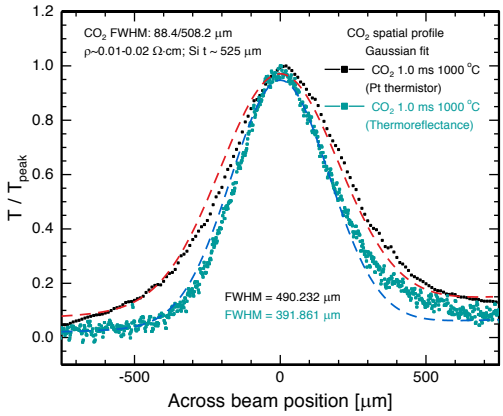

(a) Spatial profile comparison between thermoreflectance and thermistor

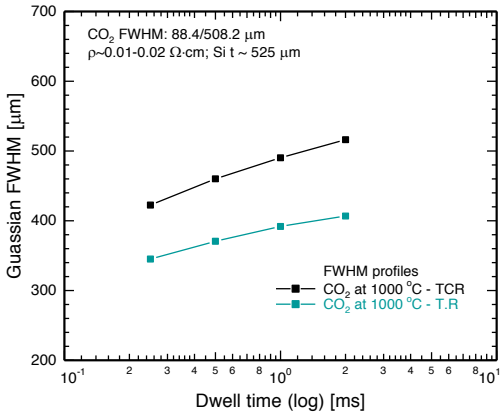

(b) FWHM comparison between thermistor and thermoreflectance for τ_{dwell} ranging from 250 to 2000 µs

Figure 5.9: Comparison of spatial profiles during CO_2 LSA (a) Spatial profiles for a 1 ms dwell. b) FWHM vs. dwell relationship for thermoreflectance and Pt resistors measurement on a logarithmic scale

The origin of this difference is unclear, and the variation may be due to calibration of the laser beam profile since Pt thermistor measurements are several years old. For the thermistor measurements, the FWHM of the laser beam was 588.2 μm, whereas the laser beam measured at the time of the thermoreflectance was only 508.2 μm. Figure 5.9 (b) shows the FWHMs plotted as a function of dwell time from 250 μs to 2 ms; the narrower profile from the thermoreflectance data is consistent for all dwells.

Temporal profiles for τ_{dwell} as a function of temperature changes are shown in Figure 5.10. Measurements match close to the thermistor results at τ_{dwell} <1 ms, but deviated for τ_{dwell} >1 ms. Similar to the previous spatial profile comparison, thermoreflectance measurements vary significantly from the thermistor measurements.

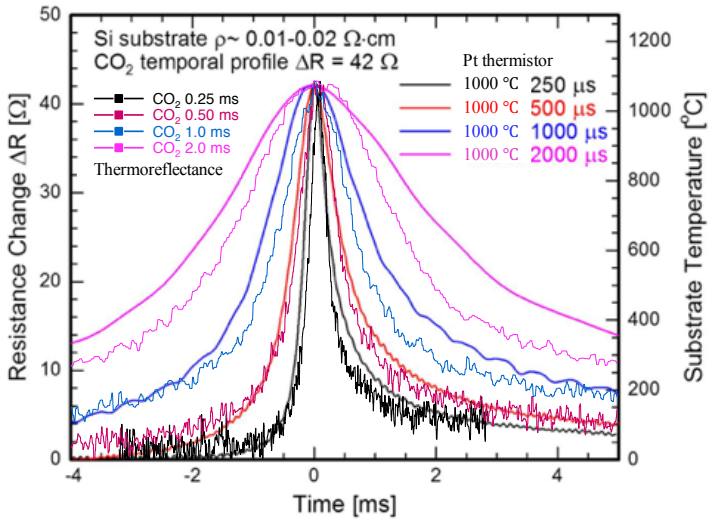

Figure 5.10: Comparison of temporal profiles for τ_{dwell} ranging from 250 μs to 2000 μs during CO_2 LSA. Pt thermistor measurements is thicker line, and thermoreflectance is thinner line

5.4.5 Comparison with Simulation Results

Temperature measurements were also compared with simulation using the Cornell Laser Annealing Simulation Package (CLASP), which was developed by Krishna Iyengar [90]. The software enables modeling of CO_2 laser absorption through free carriers and simulates that transport through during LSA [32]. Input parameters including line power density (W/cm), Si substrate reflectivity and doping concentrations which were calibrated from previous reports [91].

Temporal profiles of CO_2 LSA were simulated using CLASP and plotted in Figure 5.11 (a) along with comparable thermoreflectance profiles. The shape of the simulated and experimental profiles are in very good agreement with both leading and trailing edges consistent. The simulated data is compared with measured data as a function of τ_{dwell} from 250 μs to 2 ms in Figure 5.11 (b). While the profiles at higher dwell times are nearly identical, differences at the

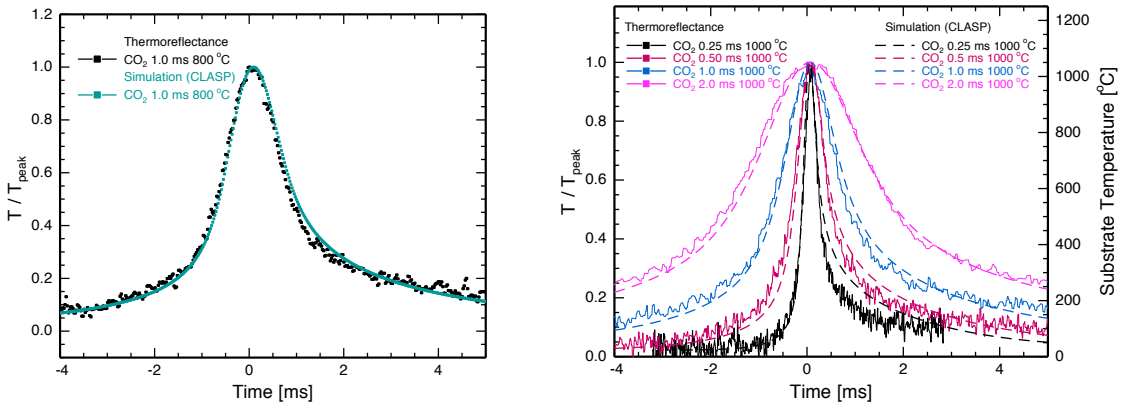

(a) Simulated temporal profile compared to thermoreflectance results

(b) Comparison between simulation and thermoreflectance for τ_{dwell} ranging from 250 to 2000 µs

Figure 5.11: Temporal profiles during CO_2 LSA (a) Simulated temporal profiles for a 1 ms dwell with thermoreflectance measurements. b) Comparison between the simulated profiles and the thermoreflectance measurements at multiple dwell times. The simulated and the measured profiles are extremely identical with a minor deviation

short dwell time should be investigated further. The strong agreement in these data is convincing evidence of the quantitative validity of the thermoreflectance extracted temperatures.

5.5 Discussions

5.5.1 Implications and Deviation from Numerical Models

The thermoreflectance implied temperature dependence to $\Delta R/R$ exhibits nearly linear behavior over temperature from 27 to 1400 °C. Theoretical models of Si optical functions suggest a linear dependence with temperature below 500

°C [81, 85]. However, data show a consistent non–linear dependence with temperatures above 1200 °C for all dwells. As mentioned earlier, the origin of this non–linearity need further investigation. The variation may arise from errors in previous temperature calibrations, impact of impurity doping for Si absorption [80], or a decrease in Si thermal conductivity at high temperatures [92]. More work is required to validate this non–linear region.

CHAPTER 6

CONCLUSIONS AND FUTURE WORKS

6.1 Conclusions

In summary, laser spike annealing of III–V and III–N was explored. Laser diode LSA enhanced and maximized dopant activation of Si–doped InGaAs to >80% of the implantation level. No deactivation was observed at high temperature for RTA–annealed samples during laser annealing. Higher annealing temperature before sample damage still remain uncertain and need to be investigated further. Dopant activation of Si-doped GaN was successful during CO_2 LSA. LOPCM shifts corresponding to active carrier concentration were identified using Raman, and observed active dopant density was higher than as-implanted. Higher activation temperature of GaN defect annealing also needs to be explored further.

CCD–based thermoreflectance imaging of Si to determine temperature profiles has been demonstrated. Black–body radiation for improving thermoreflectance SNR and thermal response calibration with linear dependence at low temperatures were investigated. Results match with previous measurements from Pt thermistor, as well as significantly well with simulation from CLASP. Results enable the rapid and direct measurements of temperature during sub–millisecond CO_2 LSA, making it powerful tool for characterizing dopant activation and metastable phase formation.

6.2 Future Works

6.2.1 Temperature Measurement on III–V and III–N Materials

In previous studies of laser-annealed III–V materials, the optimal temperature for dopant activation was very close to the damage temperature for the material. Temperature measurement on III–V materials under LSA are very difficult, but would be extremely useful for further research. Figure 6.1 (a) shows the reflectivity for various III–V materials as a function of wavelength at room temperature. Accurate temperature dependent values are not known making quantification of each material a challenge. However, the method developed in this chapter could be used for III–V materials by coating a Si thin film on top of the III–V material surface (Fig. 6.2 (b)); analysis of CCD–based thermoreflectance imaging of Si would provide spatial and temporal temperature profiles. Ultimately, this can be applied to other materials such as gallium nitride high-electron-mobility transistor (GaN HEMT) and β-Ga_2O_3 for DC (direct current) and RF (radio frequency) power device applications.

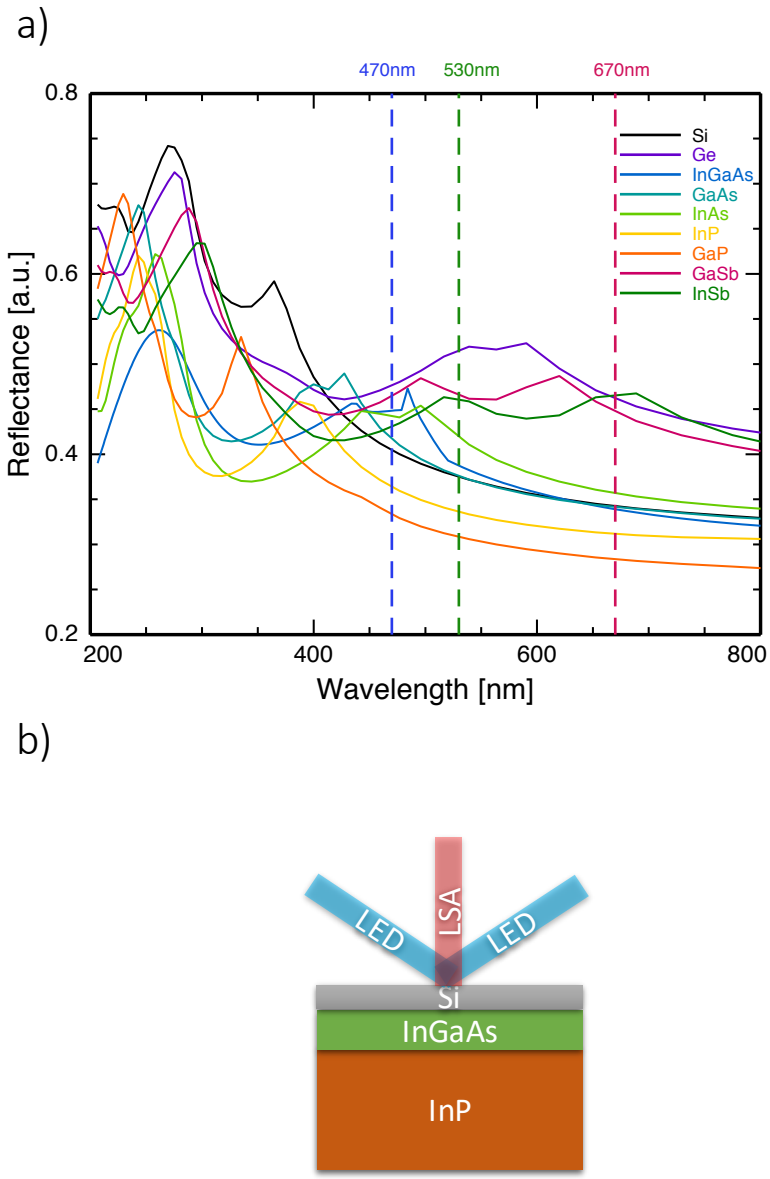

Figure 6.1: (a) Reflectance of III–V materials as a function of wavelength at room temperature (b) Scheme of temperature measurement of III–V materials using CCD–based thermoreflectance imaging method

BIBLIOGRAPHY

[1] J. Christofferson, K. Maize, Y. Ezzahri, J. Shabani, X. Wang, and A. Shakouri. Microscale and nanoscale thermal characterization techniques. *Thermal Issues in Emerging Technologies: Theory and Application*, pages 3–9. IEEE, 2007.

[2] L. Artús, R. Cuscó, J. Ibanez, J.M. Martin, and G. González-Díaz. Raman-scattering criteria for characterization of anneal-restored zinc blende single crystals: Application to Si^+-implanted InP. *Journal of Applied Physics*, 82(8):3736–3739, 1997.

[3] H. Harima. Properties of GaN and related compounds studied by means of Raman scattering. *Journal of Physics: Condensed Matter*, 14(38):R967, 2002.

[4] R.T. Bell, A.G. Jacobs, V.C. Sorg, B. Jung, M.O. Hill, B.E. Treml, and M.O. Thompson. Lateral temperature-gradient method for high-throughput characterization of material processing by millisecond laser annealing. *ACS Combinatorial Science*, 18(9):548–558, 2016.

[5] R. Cuscó, L. Artús, S. Hernández, J. Ibáñez, and M. Hopkinson. Raman scattering by LO phonon-plasmon coupled modes in n-type $In_{0.53}Ga_{0.47}As$. *Physical Review B*, 65(3):035210, 2001.

[6] J.E. Maslar, J.F. Dorsten, P.W. Bohn, S. Agarwala, I. Adesida, C. Caneau, and R. Bhat. Phonon-electron interactions in the two-dimensional electron gas in InGaAs-InAlAs modulation-doped field-effect transistor structures studied by Raman scattering. *Applied Physics Letters*, 63(14):1909–1911, 1993.

[7] S. Hernandez, R. Cuscó, N. Blanco, G. González-Dıaz, and L. Artus. Study of the electrical activation of Si^+-implanted InGaAs by means of Raman scattering. *Journal of Applied Physics*, 93(5):2659–2662, 2003.

[8] J. Ibáñez, E. Tarhan, A.K. Ramdas, S. Hernández, R. Cuscó, L. Artús, M.R. Melloch, and M. Hopkinson. Direct observation of LO phonon-plasmon coupled modes in the infrared transmission spectra of n-GaAs and n-$In_xGa_{1-x}As$ epilayers. *Physical Review B*, 69(7):075314, 2004.

[9] H. Harima, H. Sakashita, and S. Nakashima. Raman microprobe measurement of under-damped LO-phonon-plasmon coupled mode in n-type

GaN. *Materials Science Forum*, volume 264, pages 1363–1366. Trans Tech Publ, 1998.

[10] P. Perlin, J. Camassel, W. Knap, T. Taliercio, J.C. Chervin, T. Suski, I. Grzegory, and S. Porowski. Investigation of longitudinal-optical phonon-plasmon coupled modes in highly conducting bulk GaN. *Applied Physics Letters*, 67(17):2524–2526, 1995.

[11] T. Kozawa, T. Kachi, H. Kano, Y. Taga, M. Hashimoto, N. Koide, and K. Manabe. Raman scattering from LO phonon-plasmon coupled modes in gallium nitride. *Journal of Applied Physics*, 75(2):1098–1101, 1994.

[12] K. WiesenhŘtter and W. Skorupa. Low-cost and large-area electronics, roll-to-roll processing and beyond. *Subsecond Annealing of Advanced Materials*, pages 271–295. Springer, 2014.

[13] R. Ditchfield and E.G. Seebauer. Rapid thermal processing: Fixing problems with the concept of thermal budget. *Journal of the Electrochemical Society*, 144(5):1842–1849, 1997.

[14] M.V. Allmen and A. Blatter. *Laser-beam interactions with materials: Physical principles and applications*, volume 2. Springer Science & Business Media, 2013.

[15] Y. Wang, S. Chen, M. Shen, X. Wang, S. Zhou, J. Hebb, and D. Owen. Laser spike annealing for advanced CMOS devices. *Junction Technology, 2008. IWJT'08. Extended Abstracts-2008 8th International Workshop*, pages 126–130. IEEE, 2008.

[16] J. Lawrence, K.L. Pey, and P.S. Lee. Pulsed laser annealing technology for nano-scale fabrication of silicon-based devices in semiconductors. *Advances in Laser Materials Processing (Second Edition)*, pages 299–337. Elsevier, 2018.

[17] V.C. Sorg, S.N. Zhang, M. Hill, P. Clancy, and M.O. Thompson. Dopant activation and deactivation in InGaAs during sub-millisecond thermal annealing. *ECS Transactions*, 66(4):117–124, 2015.

[18] J.A. Golovchenko and T.N.C. Venkatesan. Annealing of Te-implanted GaAs by ruby laser irradiation. *Applied Physics Letters*, 32(3):147–149, 1978.

[19] B.J. Sealy, S.S. Kular, K.G. Stephens, R. Croft, and A. Palmer. Electrical

properties of laser-annealed donor-implanted GaAs. *Electronics Letters*, 14(22):720–721, 1978.

[20] S.S. Kular, B.J. Sealy, M.H. Badawi, K.G. Stephens, D. Sadana, and G.R. Booker. Laser annealing of capped and uncapped GaAs. *Electronics Letters*, 15(14):413–414, 1979.

[21] M.H. Badawi, J.A. Akintunde, B.J. Sealy, and K.G. Stephens. Effect of Si_3N_4 encapsulation on the laser-annealing behaviour of GaAs. *Electronics Letters*, 15(15):447–448, 1979.

[22] P.A. Barnes, H.J. Leamy, J.M. Poate, S.D. Ferris, J.S. Williams, and G.K. Celler. Ohmic contacts produced by laser-annealing Te-implanted GaAs. *AIP Conference Proceedings*, volume 50, pages 647–652. AIP, 1979.

[23] R.B. James, W.H. Christie, R.E. Eby, B.E. Mills, and L.S. Darken Jr. Nonlinear optical studies and CO_2 laser-induced melting of Zn-doped GaAs. *Journal of Applied Physics*, 59(4):1323–1333, 1986.

[24] E.Y.J. Kong, P. Guo, X. Gong, B. Liu, and Y.C. Yeo. Toward conformal damage-free doping with abrupt ultrashallow junction: Formation of Si monolayers and laser anneal as a novel doping technique for InGaAs nMOSFETs. *IEEE Transactions on Electron Devices*, 61(4):1039–1046, 2014.

[25] M.H. Zaldıvar, P. Fernández, J. Piqueras, and J. Solıs. Effect of laser irradiation on the luminescence of Mg and Si-doped GaN films. *Journal of Applied Physics*, 85(2):1120–1123, 1999.

[26] W.C. Lai, M. Yokoyama, S.J. Chang, J.D. Guo, C.H. Sheu, T.Y. Chen, W.C. Tsai, J.S. Tsang, S.H. Chan, and S.M. Sze. Optical and electrical characteristics of CO_2-laser-treated Mg-doped GaN film. *Japanese Journal of Applied Physics*, 39(11B):L1138, 2000.

[27] B.S. Zheng, C.L. Ho, K.Y. Cheng, C.L. Liao, M.C. Wu, and K.C. Hsieh. Improved contact characteristics of laser-annealed p-GaN coated with Ni films. *Journal of Applied Physics*, 118(8):085706, 2015.

[28] H.T. Wang, L.S. Tan, and E.F. Chor. Pulsed laser annealing of Be-implanted GaN. *Journal of Applied Physics*, 98(9):094901, 2005.

[29] T. Penna, B. Tell, A.S.H. Liao, T.J. Bridges, and G. Burkhardt. Ion im-

plantation of Si and Se donors in $In_{0.53}Ga_{0.47}As$. *Journal of Applied Physics*, 57(2):351–354, 1985.

[30] S.J. Pearton, J.C. Zolper, R.J. Shul, and F. Ren. GaN: Processing, defects, and devices. *Journal of Applied Physics*, 86(1):1–78, 1999.

[31] K. Iyengar, B. Jung, M. Willemann, P. Clancy, and M.O. Thompson. Experimental determination of thermal profiles during laser spike annealing with quantitative comparison to 3-dimensional simulations. *Applied Physics Letters*, 100(21):211915, 2012.

[32] B. Jung, J. Sha, F. Paredes, M. Chandhok, T.R. Younkin, U. Wiesner, C.K. Ober, and M.O. Thompson. Kinetic rates of thermal transformations and diffusion in polymer systems measured during sub-millisecond laser-induced heating. *ACS Nano*, 6(7):5830–5836, 2012.

[33] X. Wang, S. Farsiu, P. Milanfar, and A. Shakouri. Power trace: An efficient method for extracting the power dissipation profile in an IC chip from its temperature map. *IEEE Transactions on Components and Packaging Technologies*, 32(2):309–316, 2009.

[34] J. McDonald and G. Albright. Microthermal imaging in the infrared. *Electronics Cooling*, 3:27–30, 1997.

[35] D.D. Griffin. Infrared techniques for measuring temperature and related phenomena of microcircuits. *Applied Optics*, 7(9):1749–1756, 1968.

[36] A. Sarua, H. Ji, M. Kuball, M.J. Uren, T. Martin, K.P. Hilton, and R.S. Balmer. Integrated micro-Raman/infrared thermography probe for monitoring of self-heating in AlGaN/GaN transistor structures. *IEEE Transactions on Electron Devices*, 53(10):2438–2447, 2006.

[37] D.L. Blackburn. Temperature measurements of semiconductor devices-a review. *Semiconductor Thermal Measurement and Management Symposium, 2004. Twentieth Annual IEEE*, pages 70–80. IEEE, 2004.

[38] A. Shakouri, K. Maize, P. Jackson, X. Wang, B. Vermeersch, and K. Yazawa. Ultrafast submicron thermal characterization of integrated circuits. *Physical and Failure Analysis of Integrated Circuits (IPFA), 2012 19th IEEE International Symposium on the*, pages 1–2. IEEE, 2012.

[39] J. Kölzer, E. Oesterschulze, and G. Deboy. Thermal imaging and measure-

ment techniques for electronic materials and devices. *Microelectronic Engineering*, 31(1-4):251–270, 1996.

[40] M. Farzaneh, K. Maize, D. Lüerßen, J.A. Summers, P.M. Mayer, P.E. Raad, K.P. Pipe, A. Shakouri, R.J. Ram, and J.A. Hudgings. CCD-based thermoreflectance microscopy: Principles and applications. *Journal of Physics D: Applied Physics*, 42(14):143001, 2009.

[41] J. Christofferson, K. Maize, Y. Ezzahri, J. Shabani, X. Wang, and A. Shakouri. Microscale and nanoscale thermal characterization techniques. *Journal of Electronic Packaging*, 130(4):041101, 2008.

[42] Y. Yue and X. Wang. Nanoscale thermal probing. *Nano Reviews*, 3(1):11586, 2012.

[43] J. Christofferson and A. Shakouri. Thermal measurements of active semiconductor micro-structures acquired through the substrate using near IR thermoreflectance. *Microelectronics Journal*, 35(10):791–796, 2004.

[44] S. Shin, M.A. Wahab, M. Masuduzzaman, K. Maize, J. Gu, M. Si, A. Shakouri, D.Y. Peide, and M.A. Alam. Direct observation of self-heating in III–V gate-all-around nanowire MOSFETs. *IEEE Transactions on Electron Devices*, 62(11):3516–3523, 2015.

[45] B. Batz. Reflectance modulation at a germanium surface. *Solid State Communications*, 4(5):241–243, 1966.

[46] E. Matatagui, A.G. Thompson, and M. Cardona. Thermoreflectance in semiconductors. *Physical Review*, 176(3):950, 1968.

[47] P.W. Epperlein. Micro-temperature measurements on semiconductor laser mirrors by reflectance modulation: A newly developed technique for laser characterization. *Japanese Journal of Applied Physics*, 32(12R):5514, 1993.

[48] A.M. Mansanares, D. Fournier, and A.C. Boccara. Temperature measurements of telecommunication lasers on a micrometre scale. *Electronics Letters*, 29(23):2045–2047, 1993.

[49] P. Voigt, J. Hartmann, and M. Reichling. Thermal wave imaging of electrically heated microstructures. *Journal of Applied Physics*, 80(4):2013–2018, 1996.

[50] A. Miklós and A. Lőrincz. Transient thermoreflectance of thin metal films in the picosecond regime. *Journal of Applied Physics*, 63(7):2391–2395, 1988.

[51] B.M. Clemens, G.L. Eesley, and C.A. Paddock. Time-resolved thermal transport in compositionally modulated metal films. *Physical Review B*, 37(3):1085, 1988.

[52] D. Guidotti and H.M. Van Driel. Spatially resolved defect mapping in semiconductors using laser-modulated thermoreflectance. *Applied Physics Letters*, 47(12):1336–1338, 1985.

[53] G. Tessier, S. Hole, and D. Fournier. Quantitative thermal imaging by synchronous thermoreflectance with optimized illumination wavelengths. *Applied Physics Letters*, 78(16):2267–2269, 2001.

[54] J.A. Batista, D. Takeuti, A.M. Mansanares, and E.C. da Silva. Contrast and sensitivity enhancement in photothermal reflectance microscopy through the use of specific probing wavelengths: Applications to microelectronics. *Analytical Sciences/Supplements Proceedings of 11th International Conference of Photoacoustic and Photothermal Phenomena*, pages s73–s75. The Japan Society for Analytical Chemistry, 2002.

[55] J. Ibáñez and R. Cuscó. Raman spectroscopy of compound semiconductors. *Semiconductor Research*, pages 259–281. Springer, 2012.

[56] J. Jimenez and J.W. Tomm. *Spectroscopic Analysis of Optoelectronic Semiconductors*, volume 202. Springer, 2016.

[57] A.G. Lind, H.L. Aldridge, C. Hatem, M.E. Law, and S. Jones, K. Dopant selection considerations and equilibrium thermal processing limits for n^+-$In_{0.53}Ga_{0.47}As$. *ECS Journal of Solid State Science and Technology*, 5(5):Q125–Q131, 2016.

[58] V.C. Sorg. Laser Annealing and Dopant Activation in III-V Materials. *Cornell University*, 2017.

[59] C.G. Van de Walle and J. Neugebauer. First-principles calculations for defects and impurities: Applications to III-nitrides. *Journal of Applied Physics*, 95(8):3851–3879, 2004.

[60] J. Neugebauer and C.G. Van de Walle. Gallium vacancies and the yellow luminescence in GaN. *Applied Physics Letters*, 69(4):503–505, 1996.

[61] C.G. Van de Walle, J. Neugebauer, C. Stampfl, M.D. McCluskey, and N.M. Johnson. Defects and defect reactions in semiconductor nitrides. *Acta Physica Polonica Series A*, 96:613–628, 1999.

[62] J. Neugebauer and C.G. Van de Walle. Atomic geometry and electronic structure of native defects in GaN. *Physical Review B*, 50(11):8067, 1994.

[63] T. Mattila and R.M. Nieminen. Point-defect complexes and broadband luminescence in GaN and AlN. *Physical Review B*, 55(15):9571, 1997.

[64] C.H Park and D.J. Chadi. Stability of deep donor and acceptor centers in GaN, AlN, and BN. *Physical Review B*, 55(19):12995, 1997.

[65] T. Mattila and R.M. Nieminen. Ab initio study of oxygen point defects in GaAs, GaN, and AlN. *Physical Review B*, 54(23):16676, 1996.

[66] P. Bogusławski and J. Bernholc. Doping properties of C, Si, and Ge impurities in GaN and AlN. *Physical Review B*, 56(15):9496, 1997.

[67] D.P. Bour, H.F. Chung, W. Götz, L. Romano, B.S. Krusor, D. Hofstetter, S. Rudaz, C.P. Kuo, F.A. Ponce, N.M. Johnson, et al. Characterization of OMVPE-grown AlGaInN heterostructures. *MRS Online Proceedings Library Archive*, 449, 1996.

[68] L.T. Romano, M. Kneissl, J.E. Northrup, C.G. Van de Walle, and D.W. Treat. Influence of microstructure on the carrier concentration of Mg-doped GaN films. *Applied Physics Letters*, 79(17):2734–2736, 2001.

[69] D.C. Look, D.C. Reynolds, J.W. Hemsky, J.R. Sizelove, R.L. Jones, and R.J. Molnar. Defect donor and acceptor in GaN. *Physical Review Letters*, 79(12):2273, 1997.

[70] S.M. Myers, A.F. Wright, G.A. Petersen, C.H. Seager, W.R. Wampler, M.H. Crawford, and J. Han. Equilibrium state of hydrogen in gallium nitride: Theory and experiment. *Journal of Applied Physics*, 88(8):4676–4687, 2000.

[71] S.M. Myers, A.F. Wright, G.A. Petersen, W.R. Wampler, C.H. Seager, M.H. Crawford, and J. Han. Diffusion, release, and uptake of hydrogen in magnesium-doped gallium nitride: Theory and experiment. *Journal of Applied Physics*, 89(6):3195–3202, 2001.

[72] G. Abstreiter. Micro-Raman spectroscopy for characterization of semiconductor devices. *Applied Surface Science*, 50(1-4):73–78, 1991.

[73] M. Cazzanelli, C. Vinegoni, and L. Pavesi. Temperature dependence of the photoluminescence of all-porous-silicon optical microcavities. *Journal of Applied Physics*, 85(3):1760–1764, 1999.

[74] L. Pavesi and M. Guzzi. Photoluminescence of $Al_xGa_{1-x}As$ alloys. *Journal of Applied Physics*, 75(10):4779–4842, 1994.

[75] K. Maize and A. Shakouri. Transient thermal imaging using thermoreflectance. *Semiconductor Thermal Measurement and Management Symposium, 2008. Semi-Therm 2008. Twenty-fourth Annual IEEE*, pages 55–58. IEEE, 2008.

[76] G. Tessier, M. Bardoux, C. Boue, C. Filloy, and D. Fournier. Back side thermal imaging of integrated circuits at high spatial resolution. *Applied Physics Letters*, 90(17):171112, 2007.

[77] T. Favaloro, J.H. Bahk, and A. Shakouri. Characterization of the temperature dependence of the thermoreflectance coefficient for conductive thin films. *Review of Scientific Instruments*, 86(2):024903, 2015.

[78] D. Pierścińska. Thermoreflectance spectroscopyanalysis of thermal processes in semiconductor lasers. *Journal of Physics D: Applied Physics*, 51(1):013001, 2017.

[79] M. Farzaneh, R. Amatya, D. Luerben, K.J. Greenberg, W.E. Rockwell, and J.A. Hudgings. Temperature profiling of VCSELs by thermoreflectance microscopy. *IEEE Photonics Technology Letters*, 19(8):601–603, 2007.

[80] A. Borghesi, P. Bottazzi, G. Guizzetti, L. Nosenzo, and A. Stella. Thermoreflectance investigation of heavily doped silicon. *Solid State Communications*, 60(10):807–810, 1986.

[81] G.E. Jellison Jr and F.A. Modine. Optical functions of silicon between 1.7 and 4.7 ev at elevated temperatures. *Physical Review B*, 27(12):7466, 1983.

[82] L.D. Carlos and F. Palacio. *Thermometry at the Nanoscale: Techniques and Selected Applications*. Royal Society of Chemistry, 2015.

[83] S. Volz. *Thermal Nanosystems and Nanomaterials*, volume 118. Springer Science & Business Media, 2009.

[84] J.A. Summers, T. Yang, M.T. Tuominen, and J.A. Hudgings. High contrast, depth-resolved thermoreflectance imaging using a Nipkow disk confocal microscope. *Review of Scientific Instruments*, 81(1):014902, 2010.

[85] G. Vuye, S. Fisson, V.N. Van, Y. Wang, J. Rivory, and F. Abeles. Temperature dependence of the dielectric function of silicon using in situ spectroscopic ellipsometry. *Thin Solid Films*, 233(1-2):166–170, 1993.

[86] G.E. Jellison Jr and F.A. Modine. Optical functions of silicon at elevated temperatures. *Journal of Applied Physics*, 76(6):3758–3761, 1994.

[87] K.L. Chan. High Resolution Thermal Imaging for Electrical and Optical Characterization of Electronic and Photonic Devices. *University of Michigan*, 2007.

[88] J. Christofferson, D. Vashaee, A. Shakouri, P. Melese, and J. Baskin. High resolution non-contact thermal characterization semiconductor devices. Technical report, California University Santa Cruz School of Engineering, 2006.

[89] S.A. Thorne, S.B. Ippolito, M.S. Ünlü, and B.B. Goldberg. High-resolution thermoreflectance microscopy. *MRS Online Proceedings Library Archive*, 738, 2002.

[90] K. Iyengar. Modeling Sub-Millisecond Laser Spike Annealing Processes. *Cornell University*, 2012.

[91] B. Jung. Laser-induced Millisecond Heating of Polymers and Small Molecules for Pattern Development. *Cornell University*, 2014.

[92] H.R. Shanks, D. Maycock, P, P.H. Sidles, and G.C. Danielson. Thermal conductivity of silicon from 300 to 1400 K. *Physical Review*, 130(5):1743, 1963.